TABLE OF CONTENTS

Page

X

LIST OF TABLES

LIST OF FIGURES

LIST OF ABREVIATIONS

ADM   Absolute Distance Measuring

CCD   Charge-coupled Device

CMM   Coordinate Measuring Machine

CoRo   Control and Robotics Laboratory

CPC   Complete and Parametrically Continuous

DH   Denavit-Hartenberg

MDH   Modified Denavit-Hartenberg

PC   Personal Computer

POE   Product of Exponentials

ROSY   Robot Optimization System

SCARA   Selective Compliance Assembly Robot Arm

SMR   Spherical Mounted Retroflector

StdDev   Standard Deviation

TCP   Tool Center Point

Wrt.   With respect to

LIST OF SYMBOLS AND UNITS OF MEASUREMENT

in	inches
kg	kilograms
m, mm, μm	metre, millimetre, micrometre
$\varnothing$	Diameter
$\hat{X}, \hat{Y}, \hat{Z}$	coordinate frame axes
$x_w\, y_w\, z_w$	world coordinate frame axes
F	frame representation
F_0	robot base frame
F_6	6th axis frame
F_w	world frame
F_T	tool frame
R_x, R_y, R_z	rotation around x, y, z axes
Tr_x, Tr_y, Tr_z	translation along x, y, z axes
T_i^j	transformation matrix of the ith referential wrt. j^{th} referential
R_i^j	rotation matrix of the ith referential wrt. j^{th} referential
p_i^j	translation matrix of the ith referential wrt. j^{th} referential
c_i	coefficient value of the ith joint
τ_i	external torques applied on the ith joint
$q_i, \dot{q}_i, \ddot{q}_i$	position, speed, acceleration of the ith joint
$\omega_i^j, \dot{\omega}_i^j$	angular speed and acceleration of the ith link wrt. j^{th} link
$\dot{v}_i^j$	linear acceleration of the ith link wrt. j^{th} link

$\dot{v}c_i^i$	linear acceleration of the ith link center of mass wrt. j^{th} link
P_i^j	position vector of the ith link wrt. j^{th} link
Pc_i^j	position vector of the ith link center of mass wrt. j^{th} link
F_i^i	force vector acting on the ith link center of mass
N_i^i	torque vector acting on the ith link center of mass
Ic_i^i	moment of inertia of the ith link center of mass
f_i^i	applied force from i^{th} link to j^{th} link
n_i^i	applied torque from i^{th} link to j^{th} link
m_i	mass of ith link
G	gravitational effect
US$	United States dollars

INTRODUCTION

The difference between robot repeatability and robot accuracy is well known in academia, but industrial clients of robot manufacturers often confound the two concepts. Yet, while most industrial robots' position repeatability is 0.1 mm or better, even the smallest and most precise robot arms can make positioning errors of more than 1 mm, unless calibrated.

Robot calibration is the process of replacing the nominal mathematical model of a robot with another set of equations, which describes with less error the relationship between the joint values and the end-effector pose of the real robot. To identify the parameters of the new mathematical model (lengths, angles, elasticities, etc.), the full or partial pose of the robot end-effector is measured for various sets of robot joint values. The results are then fed to an optimization algorithm that identifies the parameters that minimize the errors between the actual pose measurements and the ones calculated using the new mathematical model.

Ideally, the calibration must be made by the robot manufacturer, who has suitable installations involving high-accuracy measurement devices, such as an optical tracker, a laser tracker, or a CMM. The main advantage of in-house calibration is that the new mathematical model is embedded directly in the robot controller. Thus, almost no extra steps or knowledge is required when using an in-house calibrated robot (in comparison to using a non-calibrated robot).

Unfortunately, not all clients realize that they need calibration. Indeed, in applications that require offline programming, such as material removal, the need for calibration might be obvious. In other applications, such as inspection, calibration might be avoided, but only by spending hours of tuning the robot path, each time a new part shape is to be inspected. Moreover, while some manufacturers do offer on-site calibration services, most must rent a laser tracker from a local provider of metrology services. However, renting a laser tracker is expensive, but also impossible to find in many geographic regions. Therefore, many researchers, both academia and industry, have worked on the development of portable, low-cost measurement tools for on-site robot calibration.

A low-cost, precise and fully automated measurement method creates an alternative to expensive measurement devices when it comes to calibrating an industrial robot. The proposed low-cost method in the thesis is designed and executed as precise as possible to validate this hypothesis. As addition, since considering precise industrial robotic applications working with full payload on their end-effector, implementation of the highest payload of the used robot is tested to create an exact calibration.

In the remainder of this thesis, Chapter 1 presents an in-depth review of robot calibration research and measurement methods used in this purpose, followed by a chapter describing the new calibration system containing a measurement device and an artifact. The robot modeling used in the calibration experimentation is explained through detailed equations in Chapter 3. Next, the joint configuration generation and the parameter identification principle is covered in Chapter 4. The identified parameters and validation results are presented in Chapter 5. Finally, the calibration analysis and a conclusion of the thesis is carried in the Conclusion and Recommendations.

CHAPTER 1

LITERATURE REVIEW

1.1 Overview

The field of robot calibration has been improving proportionally with the demand for more precise and accurate robots. A good accuracy performance end-result depends on many variables in the robot calibration experimentation. Implementing different robot models and parameter optimization techniques have been one research direction. The use of various measurement techniques has been another. External variables such as temperature, vibration and humidity also have an impact on robot accuracy and have been occasionally considered too in the calibration process.

In this chapter, the industrial robot types and their working principle are presented. Then, a description of robot calibration methods and error sources are given. Commonly used measurement devices and alternative methods used in calibration experimentations are also shown in this section.

1.2 Robot types

Industrial robots can be classified according to several criteria, but the most common is their architecture (the arrangement and types of their joints). The most popular members of this classification are articulated robots, Cartesian robots, SCARA robots, cylindrical robots, spherical robots and parallel robots (mostly, so-called Delta robots).

Six-axis articulated robots are the most commonly used robots in industrial applications. The advantages of articulated robots are their wide versatility and high flexibility (Hanafusa *et al.*, 1981). Some parallel robots are considered to have better accuracy and larger payload capacity (Filion, 2015). Delta robots are known for their fast-parallel movements. SCARA robots are generally used in assembly tasks (Urrea *et al.*, 2016).

1.3   Robot calibration and error sources

Finding better robot parameters different from the nominal model represents a calibration procedure to decrease the absolute position error of industrial robots. These errors are caused by geometric and non-geometric sources inside the robot model. There are three levels of calibration which are defined according to these error sources. A level-1 calibration improves the joint level errors, where level-2 calibration includes every geometric error source into consideration (Conrad *et al.*, 2000). The level-3 model takes non-geometric stiffness errors into account in addition to other levels. (Gong *et al.*, 2000).

1.3.1   Geometric errors

Geometric errors are caused by machining and assembly tolerances. These are the Denavit-Hartenberg (DH) parameters, i.e., the link lengths, twists and offsets, and the joint offsets. For example, the joint offsets are caused by unavoidable errors in the installation of the joint encoders with respect to the joint reference (zero) position. The geometric errors also include errors in the base and tool reference frames. According to Judd and Knasinski (1990), geometrical errors have the most prominent effects on the complete robot position accuracy.

1.3.2   Non-geometric errors

Non-geometric errors are considered as all other variations. The most common example is the stiffness of the gearboxes (generally modeled as linear). However, other non-negligible examples are the stiffness of the robot links and the thermal expansion of the robot components.

1.3.3   Level-1 calibration

Level-1 calibration (also called mastering) aims at correcting the offsets that happen at the robot joint level. These offset parameters have the most significant impact on accuracy improvement, according to Heping *et al.* (2008), when calibrating a six-axis articulated robot.

Indeed, every robot manufacturer provides procedures for mastering the robot, and these need to be executed every time the robot's battery is dead.

1.3.4 Level-2 calibration

Level-2 calibration identifies every geometrical error parameter from the robot's kinematic model. This level of calibration includes the error modification of joint level (Level-1) calibration.

To date, numerous level-2 calibration experiments have been performed using different mathematical models. Differences in equations and parameters between kinematic modeling methods affect the accuracy when performing level-2 calibration. In the case of articulated robots, Hayati (1983) is an example of the studies covering all kinematic parameters with a specific modeling method.

1.3.5 Level-3 calibration

Non-geometrical errors are improved in Level-3 calibration. Usually, for successful accuracy improvement, all calibration levels are combined to identify geometrical and non-geometrical error parameters. Various dynamic modeling principles have been implemented throughout this level of calibration to complete the robot identification model.

The Newton-Euler algorithm was used by Khosla and Kanade (1985) to identify the joint stiffness coefficient exerted through moments and forces. Thermal expansion related parameters were identified by Gong *et al*. (2000) through observing the changes related to the effect of thermistor sensors. Nubiola and Bonev (2013) and Feng *et al*. (2013) uses a torsional spring model to identify the joint stiffness parameters, and Lightcap *et al*. (2008) uses an additional cubic spring coefficient implemented to the same model for its identification. An elasto-geometrical calibration model was presented by Kaveh *et al*. (2016) identifies the non-geometric error parameters by observing multidirectional external loads applied to the joints.

1.4 Absolute vs. relative accuracy

According to Whitney *et al*. (1986), robot accuracy is targeted through forward or inverse, absolute and relative calibration approaches.

Relative accuracy is targeted to calibrate the robot with respect to a user reference frame defined through a set of joint values. Li *et al*. (2018) experimented calibration with a parallel robot for relative accuracy achievement by defining the user frame through reflector sensors fixed on the robot end-effector.

Absolute calibration aims to improve absolute accuracy by defining a world reference frame with respect to the robot base's actual location. The parameters concerning the world reference frame with respect to the robot base frame are also taken into identification. Nubiola and Bonev (2013) calibrated a robot with six degrees of freedom by defining the reference frame by placing and measuring three spherical mounted retroreflectors (SMR) with a laser tracker.

1.5 Classification of calibration methods

Robot calibration is classified into two methods as open-loop and closed-loop methods. The measurement instrument functionality plays a crucial role in the classification of the calibration procedure. Open-loop methods tend to use external measurement devices, and closed-loop methods usually implement physical constraints inside the robot system.

1.5.1 Open-loop calibration

The frequent use of external measurement devices is implemented to open-loop methods due to its benefits of high accuracy and measuring the ability of a large workspace volume. These positive outcomes of the method usually allow good accuracy improvement but also come with some disadvantages, such as time-consuming training requirements and high costs (Filion *et al.*, 2018).

1.5.2   Closed-loop calibration

Closed-loop or also known as self-calibration methods, rely on the data obtained through internally implemented devices constrained inside the robot system. Usually, devices such as cameras, sensors and probes are implemented to the robot end-effector for measurement purposes. External measuring devices are not tended to be used in self-calibration methods, so it is likelier to carry-on low-cost experimentation compared to open-loop methods (Gaudreault *et al.*, 2018).

1.6   Robot calibration procedure

Four main steps are usually used in robot calibration procedures (Bernhardt and Albright, 1993). Robot modeling, generation and measurement of configurations, parameter identification and compensation.

The procedure starts by modeling the robot where nominal kinematic and non-geometrical characteristics are obtained followed by multiple robot configurations generated for measurement purposes. After measurement collections, the identified new parameters are obtained through optimization, and the last step is implementing the new parameters to the robot system for accuracy improvement. Multiple variations of these steps have been used over time and presented in the sections below.

1.6.1   Modeling

Various modeling techniques have been used throughout time, each of them with different characteristics and advantages affecting the calibration procedure. The robot modeling presents the geometry of a pose to be carried out through all possible joint configurations. Kinematic redundancies in modeling are usually considered due to the possibility of forming a pose through different joint configurations. Finally, similar parameters between techniques can be implemented through geometric models in the case of a specific equivalency. Modeling

technique examples used in robot calibration procedures are presented in the following subsections.

1.6.1.1   Denavit-Hartenberg model

The Denavit-Hartenberg (D-H) convention is the most commonly used robot modeling technique proposed by Denavit and Hartenberg (1955). The principle of the technique is creating a kinematic chain with respect to a reference frame through obtaining transformations of consecutive links attached via joints. These consecutive links of the manipulator are formed through four parameters in order to get a transformation matrix. Khalil and Gautier (1985) and Hayat *et al*. (2013) are examples of works that used the D-H convention for their robot parameter identification. However, the D-H models have a drawback in the case of two consecutive parallel axes, which is the case of most six-axis industrial robots. Small errors in the parallelism of these axes lead to enormous errors in some of the D-H parameters., as first pointed out by Hayati and Mirmirani (1985).

1.6.1.2   Modified Denavit-Hartenberg model

Modified Denavit-Hartenberg (MDH) model was presented in Craig (2005), which uses the same four parameters as the DH model with some slight differences considering the location of the parameters and their transformation orders. Also, an extra parameter β was added in Hayati *et al*. (1988) to this particular model for the identification of the consecutive parallel axes. The robot presented in this thesis is modeled per MDH convention.

1.6.1.3   S model

The S model was used as a modeling technique for six identification parameters by Stone *et al*. (1986). Due to the high number of parameters involved, it is considered a suitable and less restrictive identification for parallel axes. After the identification of these parameters, it is possible to convert the S model to the DH model.

1.6.1.4   CPC model

The complete and parametrically continuous (CPC) modeling technique was used by Zhuang *et al*. (1993) and claims to be a versatile alternative modeling method for parameter identification. The error model eliminates robot singularity problems in consecutive parallel axes with a different parameter transformation principle where each link relates to three translations and one rotation. The CPC model and their identified parameters can be easily implemented in the DH model.

1.6.1.5   POE model

The Product of Exponentials (POE) formula is claimed to be a convenient way to generate a kinematic robot model automatically. Chen and Young (1997) presented it by calibrating two open-chain robots. A more robust and singularity free local POE modeling method was also proposed by Chen *et al*. (2001) with a different reference frame placement than the previously applied POE method.

1.6.2   Generation of optimal configurations

Choosing an optimal set of joint configurations plays a critical role during parameter identification. These generated optimal joint configurations are used in the measurement collection phase of robot calibration. Usually, a singular value decomposition of a systems identification matrix (Klema and Laub, 1980) is used in equations while choosing an optimal joint set.

According to Driels and Pathre (1990), it uses an inverse condition number calculated from the robot's identification jacobian matrix. The numerical change of this condition number was analyzed to determine the optimal joint set for a better accuracy improvement. Kucuk and Bingul (2003) used a global conditioning index and a condition number from the identification matrix. However, the condition number ended up successful only in limited manipulators

because of its use in local performance. They claimed that the condition number wasn't a good enough criterion for the joint configurations end-result comparison.

Observability index calculations are widely used while choosing an optimal joint set. There are different equations of indices used over time through the values of the identification matrix. Five different observability index equations have been researched and compared overtime in calibration experimentations. The first index O_1 was used by Borm and Meng (1991), where we see the use of all the singular values of the identification matrix. The observability index O_2 or also known as the inverse condition number per Driels and Pathre (1990), uses the minimum singular value divided by the maximum singular value in its equation. Nahvi *et al.* (1994) defines an observability index O_3 from the minimum singular value, Nahvi and Hollerbach (1996) calculates an O_4 index equation defined from the multiplication of the O_2 and O_3 equations. The final observability index O_5 was presented in Sun and Hollerbach (2008a) to minimize the variance of parameters. Sun and Hollerbach (2008b) analyzed a comparison between these five observability indices and claimed that the minimum singular value O_3 was the optimal index for configuration selection. However, Horne and Notash (2009) does not recommend using O_3 as the best solution in their index comparison. The recent comparison between these five observability indices were tested on a six-axis industrial robot by Joubair *et al.* (2013). The results claimed O_2 as the best optimal index for geometric calibration, but when adding joint stiffness parameters for a complete level-3 calibration, O_1 becomes the best optimal index. O_1 index is used in this thesis for the selection of the optimal joint configurations.

1.6.3   Measurement devices and methods

Measurement methodology directly affects the parameter identification step in robot calibration. Researchers have been using variations of these devices with different characteristics and advantages. They are witnessed in the data collection of calibration experimentation and categorized as external and internal measurement devices.

External devices tend to be higher in cost, but effective in calibration performance. Internal devices are integrated into the robot system, and usually placed inside of the robot manipulator or end-effector. They usually have a smaller workspace volume than external devices. Measurement devices used in calibration research overtime and examples of commercialized calibration solutions are presented in the subsections of this section.

1.6.3.1 Laser Tracker

Laser tracking methods have been commonly used over time by researchers to calibrate their robots. The principle in this methodology usually uses interferometers and collects measurements with non-contact laser beams. The first laser beam stays in the interferometer, while the second beam reflects and deflects from an SMR (spherically mounted retroreflector), which is essentially an assembly of three perpendicular mirrors embedded in a precision sphere and intersecting at its center. The interference of these two beams gives us a precise measurement.

Lau *et al.* (1985) applied a position and orientation measurement to a robot with two different laser tracking systems. Afterwards, works from Newman *et al.* (2000), Alici and Shirinzadeh (2005), and Aoyagi *et al.* (2010) showed an implementation of the laser tracker interferometer into calibration experiments. Slamani *et al.* (2012) compares an interferometer laser tracking system to an absolute distance measuring (ADM) laser tracker in their experiments. ADM is considered to be less precise than interferometer technology. However, the requirement of having continuous visibility of the SMR is a severe drawback for interferometers. Another experiment carried on by Nubiola *et al.* (2013) improved the accuracy of a serial robot without using the interferometer technology available in their laser tracker system.

Laser trackers are precise and useful measurement devices in accuracy improvement. However, they have some disadvantages such as its high equipment cost and sensitivity to external conditions. An example of a FARO ION laser tracker is shown in Figure 1.1.

Figure 1.1 FARO ION laser tracker
(image taken from www.faro.com)

1.6.3.2   Coordinate measuring machine (CMM)

Coordinate measuring machines are widely used in metrology required calibration experiments. A spherical probe is mounted to the contact end-effector and it can move along three axes inside the CMM's coordinate system. Some examples of robot calibration experiments using this method are Driels *et al.* (1993) and by Lightcap *et al*. (2008). Even though CMM's are considered to have high accuracy, the challenge of this method is the requirement of moving the robot outside of its workspace to collect measurements.

1.6.3.3   Cameras

Researchers have included different camera systems throughout their calibration measurements. Either implementing as an internal sensor, or either as an external measurement instrument.

We start seeing a charge-coupled device (CCD) camera used in accuracy improvement as an internal device mounted to the robot end-effector in Puskorius and Feldkamp (1987). Bennett

et al. (1991) presents a stereo camera as an internal device, aiming to calibrate the camera parameters to obtain a better complete system accuracy improvement. Zhuang *et al.* (1995) uses a monocular camera and identifies the robot parameters along with two extra camera parameters.

Jang *et al.* (2001)'s calibration research used an optical camera OPTOTRAK by Northern Digital Inc. as an external measurement instrument. Nubiola *et al.* (2014) also used an external camera C-track by Creaform and compared its calibration results with a laser tracker calibration. In this work, the optical camera was as good in accuracy improvement as using their laser tracker. Lastly, the thesis presented by Filion (2015) analyzes a robot calibration with a portable photogrammetric camera MaxSHOT 3D by Creaform.

1.6.3.4   Other methods

Ballbars. They measure the displacement through a telescopic sensor. Even though the drawback of only being able to measure the offset manually, it is considered a highly precise method while calibrating a robot. One of the first works to use the ballbar as a measuring tool is seen in Driels (1993). Work of Nubiola *et al.* (2013) presents an approach using a hexapod principle where a Renishaw QC20-W ballbar was used in their calibration experiments.

Planar or spherical constraints. Using constraints as measurements are found to be accurate inside the limited workspace and obtaining accurate measurements in the robot's whole workspace is still a current research subject. Joubair and Bonev (2015a) used the planar constraining technique by placing a granite cube probed with the robot tool. Joubair and Bonev (2015b) used again the constraining technique, however this time sphere probing was used in their experiments. In Nadeau *et al.,* (2019)'s paper, a collaborative robot was calibrated through the implementation of geometric constraints along with integrating an impedance control principle to the method. The first model of the TriCal measurement tool presented in Gaudreault *et al*., (2018) also uses spheres in the workspace platform, however constraining the robot TCP is achieved through coinciding with the center of the sphere by automatically

dragging towards it. The TriCal principle from this method was presented in this thesis with a new mechanical design and several improvements, along with a new design of a workspace artifact containing spheres in different planes.

Portable measurement arms. This method is not considered the ideal method for measurement data collection, but it has been used in accuracy improvement, such as in Joubair *et al.* (2012) study. They have used a portable arm from FARO Technologies, which was proven to calibrate the robot in a less complicated manner for robot users.

1.6.3.5   Commercially available devices

Since robot calibration solutions becoming more accessible and available for most robot users, different design and concept examples have been commercialized throughout time. A measuring device initially presented in Beyer and Wulfsberg (2004), uses a calibration sphere for the robot to probe along with two CCD cameras for their error measurements. The device is called ROSY and available in the market by Teconsult GmbH (Figure 1.2).

Figure 1.2 ROSY device and calibration sphere
(image taken from https://www.teconsult.de/produkte/rosy/)

Wiest AG presents a device called LaserLab, as seen in Figure 1.3. Even though its concept of measuring an position error is similar to that of the ROSY, this device uses five laser triangulation sensors meeting at a common center. However, the accuracy of these devices is still challenged compared to other available robot calibration measurement tools. In addition to these, other commercially available calibration devices have been presented, such as the Trinity probe by IBS Precision Engineering. Even though this device is considered more accurate then the ROSY and LaserLab, it is only used to calibrate machine tool axes, making it incompatible for industrial robots.
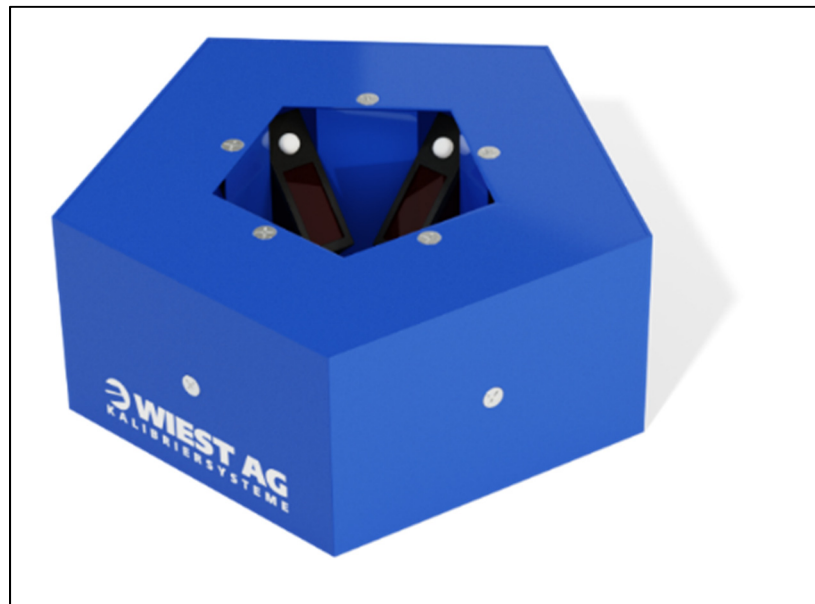
Figure 1.3 LaserLab presented by Wiest AG
(image taken from https://www.wiest-ag.de/en/laserlab.html)

1.6.4   Parameter Identification

After measurement data collection, identifying the new parameters of the robot is the next step for robot calibration. These new parameters are implemented to the robot model and the position errors are observed throughout the model. The parameters implemented to the robot are iterated through an optimization algorithm to obtain the best parameters for the desired robot accuracy.

Various optimization algorithms have been used to identify calibration parameters. The most common is the least-squares method, where the sum of the square errors from the collected measurements is minimized. Different least-squares methods have been used over time. The ordinary or linear least squares principle is used for linear regression fit through linearizing the manipulator system equations around nominal parameters. Schroer *et al.,* (1997), Pott *et al.,* (2007), Kamali *et al.,* (2016) are examples who have used linearization techniques for their manipulators before applying the optimization. Gander *et al.,* (1994) uses the Gauss-Newton least-squares method, which is another way to optimize non-linear systems. The gradient method aims to find the local minimum of differentiable functions, such as in Khalil *et al.,* (1991). The Levenberg-Marquardt or damped least-squares presented by Levenberg (1944) and Marquardt (1963) is considered to apply the combination of the Gauss-Newton and gradient methodology. Khalil and Besnard (2002) used the damped least-squares method for an industrial robot, and Kastner *et al.,* (2015) used this method for a NAO humanoid robot. An example work from Zak *et al.,* (1994), replaces the ordinary least square with a weighted least squares optimization method, which can take place when an assumption of the constant variance of errors is violated.

Other algorithms used in calibration experiments is the Kalman filter optimization used in Nguyen *et al.,* (2013), where the advantage in this method is the statement of a better uncertain noise identification. Nguyen *et al.,* (2015) again uses this method for geometric calibration. However, the non-geometric parameters were identified through an artificial neural network. The Nelder-Mead algorithm presented by Nelder and Mead (1965), was used as optimization algorithm for a robot calibration measurement with a laser tracker in Nubiola (2011). This method is considered advantageous for the optimization of unconstrained variables. Lastly, we see a parallel robot parameter identification through the Monte-Carlo method in Jokiel *et al.,* (2001).

1.6.5   Compensation

After obtaining new parameters, the robot achieves a more precise mathematical model. Ideally, better accuracy can be achieved by parameter compensation through implementing the new model to the robot controller. However, access to controllers are usually not possible for robot users real-time adjustments. An example of calibration compensation method was shown on a delta robot by Savoure *et al.,* (2006). To solve this problem, the fake pose method of Geuens *et al.,* (1997) is usually applied by researchers to validate the accuracy of the new robot model. The method calculates joint configurations from desired targets with the inverse kinematic of the new model. Next, these configurations are used for forward kinematic calculations inside the nominal kinematic model. The compensation gives us the position target errors, and the aim is observing the approach of the fake target towards the desired target. This methodology is used in this thesis due to the robot manufacturer's controller limitations.

1.7   Summary

This chapter aimed to cover the methodology and general aspects of robot calibration. Due to the requirement of high accuracy for industrial applications showed us a variety of methods searched and analyzed by robotic researchers. First, the robots used in the industry and their possible sources of error were presented, followed by the description of different methods for standard calibration procedures. Lastly, measurement devices used in these procedures were analyzed with their advantages and disadvantages. While seeking accuracy improvement, it is safe to say that robot users are looking for numerous characteristics in their calibration procedures and the devices used for measurement purposes. Efficiency, cost, simplicity, consistency, and ease of implementation are just some examples to encounter. These procedure alternatives experimented throughout time prove to us the demand and need to find an optimal method and measurement device for good end-result accuracy of industrial robots.

CHAPTER 2

THE CALIBRATION SYSTEM-TRICAL AND 3D BALL ARTIFACT

The description of an automated calibration system containing a measurement device and a fixture workspace are presented in this chapter of the thesis. Initially, the system components are defined and presented, followed by an explanation of the calibration measurement procedure and an analysis of the system's accuracy.

2.1 Description of the calibration system

The calibration system contains a portable measurement device acting as the robot tool and a rigid artifact fixture as the robot workspace. This system works in a closed-loop calibration manner, such as the tool attached as an internal device to the robot flange uses a dragging technique after having physical contact with 1-in diameter datum balls contained in the artifact fixture. Figure 2.1 shows the new device, where the artifact fixture is partially visible with one of the datum balls along with the tool mounted as the robot end-effector. The absolute position data of the measurements are obtained by calculating equations of the robot kinematic loop (presented in Chapter 3) obtained through this physical constraint to be used in the next steps of calibration. The measurement device is called TriCal, and the fixture workspace is presented as the 3D ball artifact.
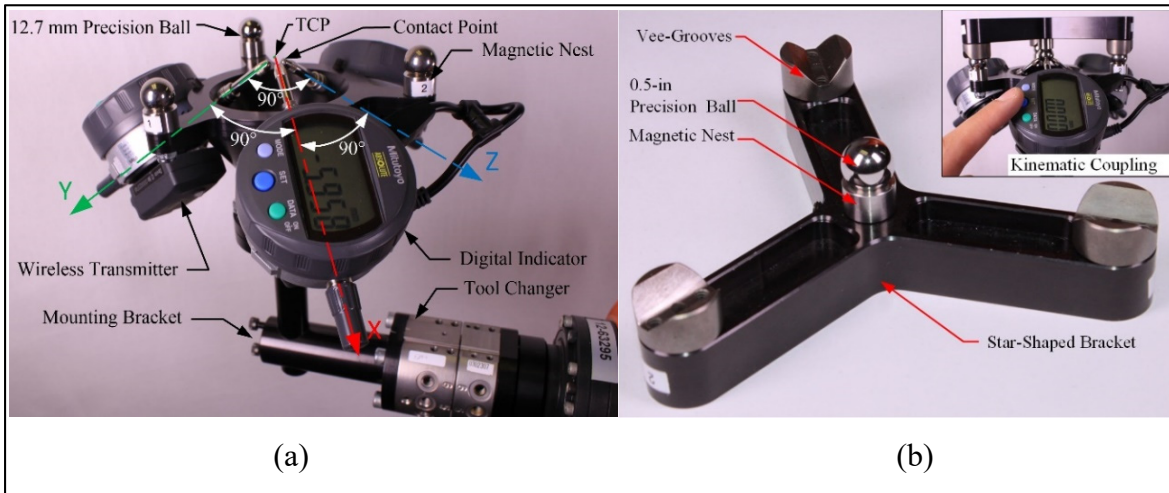
20

Figure 2.1 Old prototype of TriCal: (a) the main device and (b) its calibrator fixture
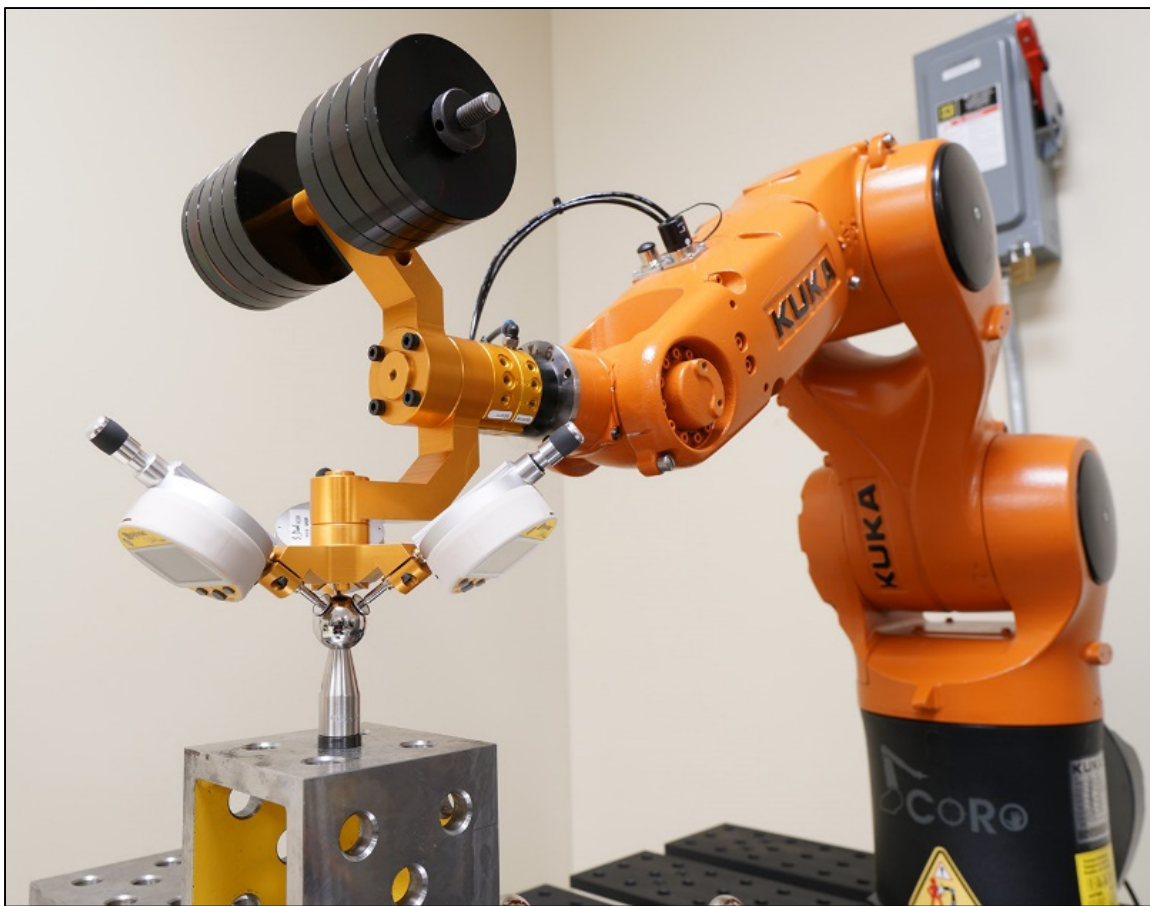
Figure 2.2 Novel prototype of TriCal

2.2   The TriCal measurement device

The initial prototype design of the TriCal measurement device (Figure 2.1) and its working principle were first presented in Gaudreault *et al*. (2018), where its calibration performance was tested on a small six-axis industrial robot (ABB IRB 120). In this thesis, the measurements are taken with a new, improved design of the TriCal. The latest model of the TriCal (Figure 2.2) was developed in the CoRo laboratory with several major improvements over the first design. The new design does not need an additional fixture for TCP initialization, and it is possible to add either 0.5 kg or 1 kg weights (steel disks) to the device.

The main part of TriCal is an aluminum triaxial mount with three $\varnothing$8-mm cylindrical channels with clamps. The axes of these channels are orthogonal and intersect at one point, which is defined as the robot TCP. Sylvac S_Dial WORK NANO digital indicators are fixed to each of the three channels. Each indicator has an accuracy of 1.8 μm and a measurement range of 12.5 mm. A disk-shaped tip of 11.5 mm diameter is attached to the tip of the indicators, thus enabling plane-sphere contact with a ball. Each indicator measures the x, y or z coordinate of the center of a ball with respect to the tool reference frame.

A 1.5-in master ball with a larger diameter than the datum balls is used for the digital indicators mastering and the TCP definition. For a convenient implementation of the master ball (Figure 2.3a), a kinematic mount in the form of a trihedral socket is directly embedded in the center of the triaxial mount in the new design of the TriCal (Figure 2.3b). Thanks to this master sphere and trihedral socket, we no longer need an additional fixture as in the first design of TriCal.
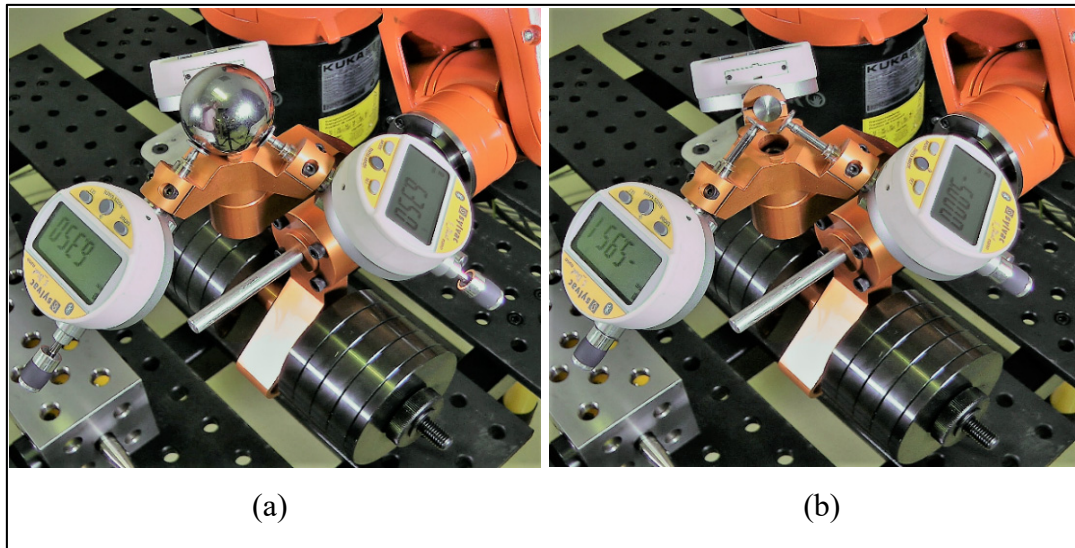
Figure 2.3 TriCal during mastering with the 1.5-in master ball

When the master ball is placed in the socket, the center of the ball defines the TCP and allows all digital indicators to be mastered. Furthermore, a removable rare-Earth magnet can be placed in the socket (Figure 2.4a), thus retaining a 1.5-in ball when needed. This magnet is only used when measuring with a CMM the coordinates of the TCP with respect to the mounting surface of TriCal, by probing the master ball, and for attaching a 1.5-in SMR during measurements with a laser tracker (Figure 2.4b). While mastering, it suffices to orient TriCal upwards and the magnet is not needed; the force of gravity acting on the master ball is much larger than the equivalent of the three-digital indicator's forces.
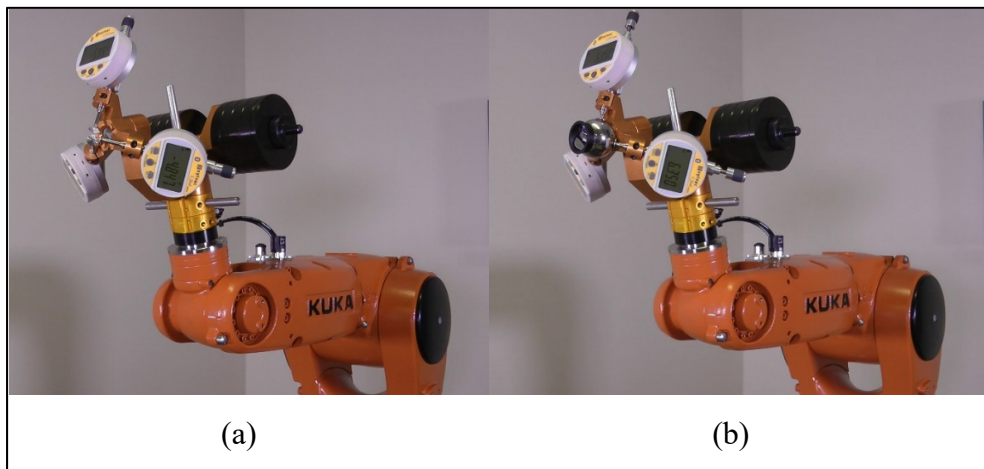
Figure 2.4 1.5-in SMR implemented to the TriCal with a rare-Earth magnet

The master ball diameter is chosen to be identically sized with the SMR used in the laser tracker validation experiments (as will be explained in Chapter 5). Datum balls with the diameter of 1 inch were chosen to be implemented to the 3D ball artifact and measured with the TriCal. These two ball sizes give us a difference in their radii of 6.350 mm. Since we want the indicators to display "0" in free mode, when the master 1.5-in ball is placed in the socket, each indicator must be set to display the radii 6.350 mm difference.

The remaining elements of TriCal are an aluminum mounting bracket for the triaxial mount that ends with a QC-11 tool changer from ATI Industrial Automation Inc., and another aluminum mounting bracket for optional steel weight disks. Thus, the total weight of the TriCal can range from 1.3 kg to 7 kg. This weight adjustment helps the TriCal adapt to calibration experimentations using the full payload of the robot.

2.3   The 3D ball artifact

The 3D ball artifact is essentially a very rigid fixture with several 1-in datum balls positioned at precisely known locations in space (not just in one plane). It was designed and implemented according to specific criteria that could affect the calibration procedure, such as the datum ball distribution on the fixture body, the artifact precision, and its portability, compactness and size. Figure 2.5 illustrates the final design of the artifact. The components, its datum ball location placement and the fixture precision itself are presented in the following subsections.
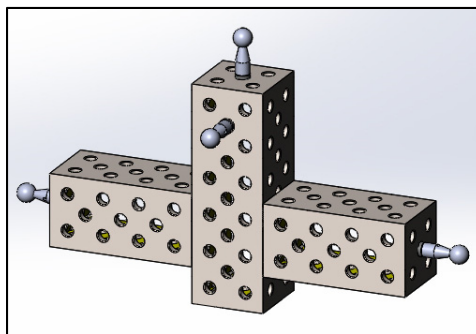
Figure 2.5 The 3D ball artifact

2.3.1 Components of the artifact

All industrial robots in the CoRo lab are installed on Valtra Steel BuildPro welding tables with precision holes and compatible riser blocks for accurate installations. Specifically, the BuildPro heavy-duty riser blocks come in 4×4×12 inches (7.8 kg) and 4×4×8 inches (5.7 kg) versions (Figure 2.6) and were deemed perfect for building the body of the 3D ball artifact. The datum balls are manufactured by Micro Surface Engineering, made from stainless steel, and readily available in diameters of 0.5 in, 0.75 in, and 1 in. As already mentioned, the 1-in datum ball (Figure 2.7) was chosen to match the 12.5 mm measurement range of the digital indicators (the difference in the radii of the master and datum balls being approximately half that range). Finally, after completing a final design, since there is a need for a world reference frame measurement during the calibration procedure, it is possible to implement three 1.5-in ball magnetic nests to create such a frame and measure it. This frame is used to locate the 1-in datum balls precisely and obtain their position information with respect to it. The 1.5-in magnetic nests are selected for this purpose since a laser tracker will measure the reference frame with a 1.5-in SMR while validating the calibration performance. This measurement during the validation step is explained in Chapter 5.

Figure 2.6 5.7-kg and 7.8-kg
BuildPro heavy-duty riser blocks
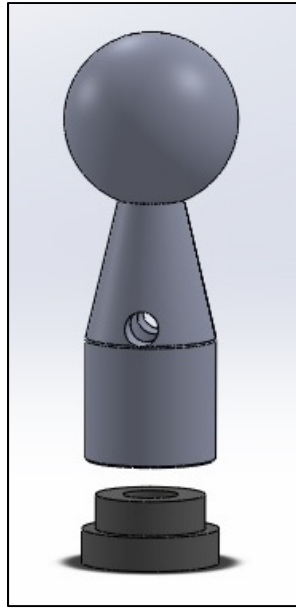
Figure 2.7 1-in datum
ball on a stem

2.3.2 Design and location placement of the artifact

Before coming up with a good artifact assumption, specific body and datum ball positioning examples are experimented with several designs and their different positioning with respect to the robot base. Initially, to get a proper calibration procedure with the artifact components presented in the previous subsection, several designs were implemented to the robot workspace. These initial designs were measured with portable equipment from FARO Technologies, the FaroArm Platinum (seen with one of the example initial designs in Figure 2.8). This metrology device was used because it is an easily accessible tool at our lab compared to a CMM, which was not always possible to use for measurement. Plus, even though the point to point accuracy of the FaroArm (close to ±18 μm) is worse than a traditional CMM, the volumetric accuracy was good enough to get an idea about an artifact measurement and the calibration procedure.
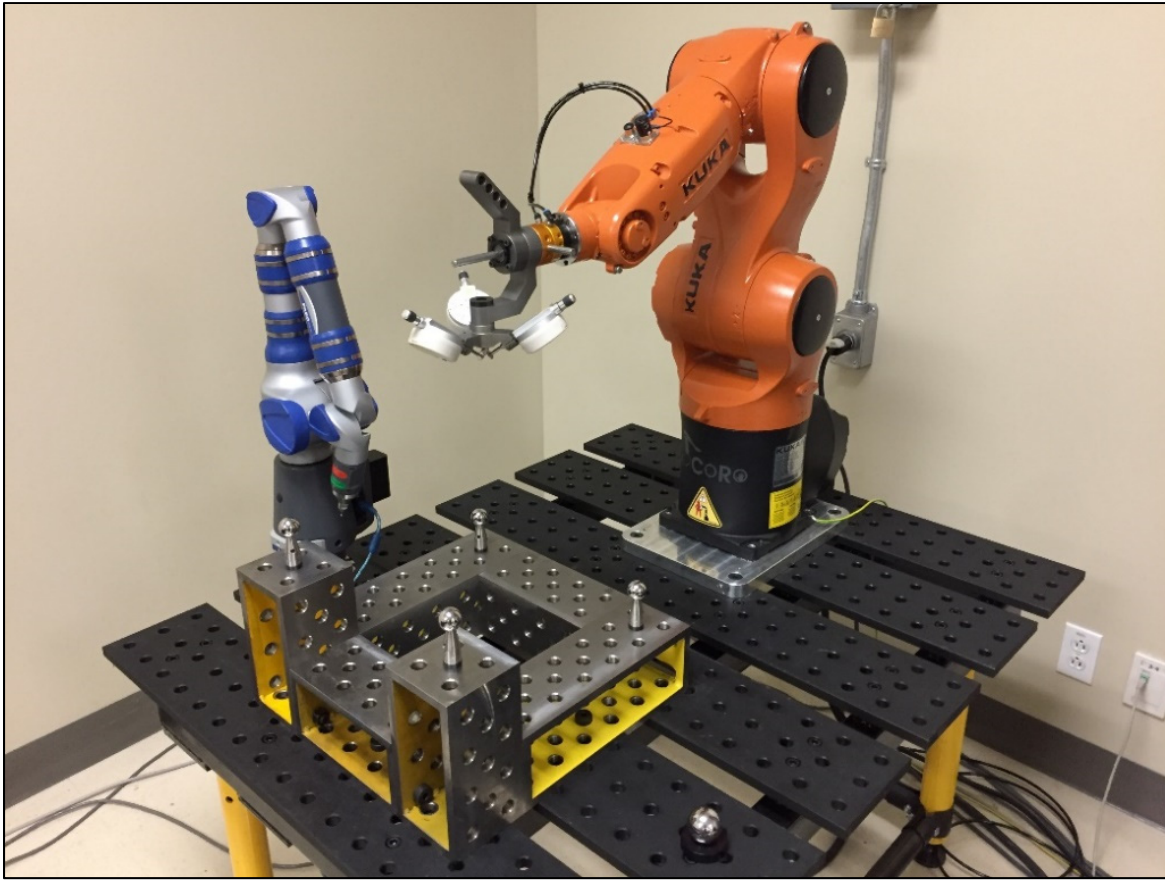
Figure 2.8 FaroArm ready for an artifact measurement

Since the workspace distribution plays a critical role in the calibration performance, the initially designed artifacts mostly contained a wide distribution of datum ball placements that were aimed to be implemented to the final design of the artifact. Even though having a larger volume surface of the artifact mating to the robot table means a steadier and well-fixed workspace, it is not sufficient to implement this as a specification for our cause, since there is an increase in the dimensions and the weight of the artifact itself. As a characteristic, the desire is to have a portable artifact that could be carried and removed by a human operator, along with a compact design that fits inside a medium-size CMM, considering the artifact should be precisely measured prior to starting the calibration procedure. The decision regarding the number of riser blocks is chosen according to these characteristics. First, to obtain a portable workspace, the complete artifact should not exceed the lifting and handling safety limit, which is approximately 23 kg in most regions. In this case, two light blocks and one heavy block is

used for assembly, weighing 20 kg approximately to keep up with this safety limit. Next, to obtain a durable and compact assembly, these two lighter riser blocks are vertically placed to the heavier riser block symmetrically.

The vertical location of these two lighter riser blocks and the possible datum ball location distribution were selected through discretization and simulation in RoboDK (offline simulation and programming tool for industrial robots), along with some practical considerations. The analysis is made with a complete calibration procedure algorithm with a fixed number of simulated joint configurations. The lowest bottom vertical placement wasn't considered into simulation due to collision reasons with the robot cell table causing joint limitations. The first two datum balls are constraint to be placed towards the edge of the smaller block planes. This idea captures a larger robot workspace with options of expanded joint displays (especially in joint axes 1). Some examples of light block implementations to a surface fixed heavy block and datum ball location examples have been illustrated in Figure 2.9.
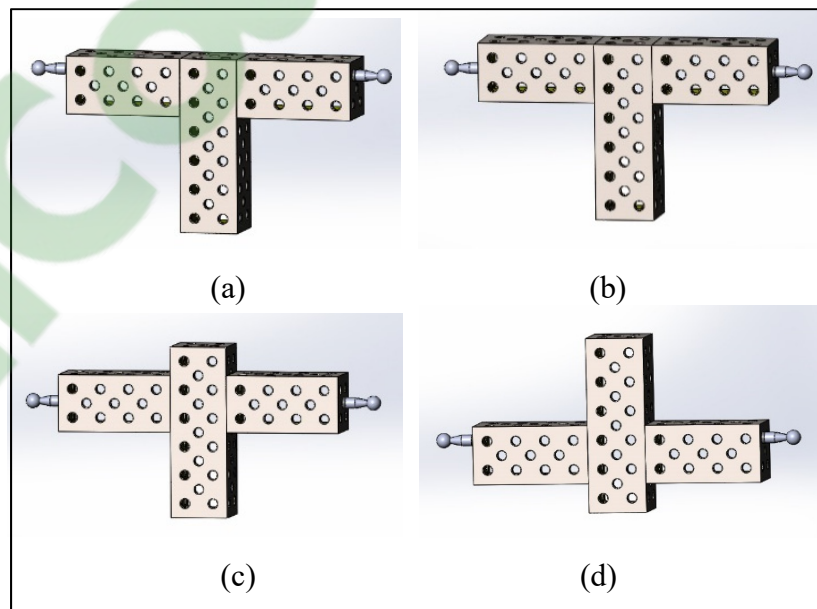
Figure 2.9 Examples of 3D ball artifact

The location placement of the artifact assembly itself with respect to the robot base is decided through the possible location of the edge balls' reachability. It minimizes robot singularities while measurement, such as in Figure 2.10.

We observed that the first two datum sphere locations after a simulation test allowed us to obtain a wider limit of joint choices in the robot's first axes compared to vertically higher locations. After fixing the light blocks to the heavy block and two edge balls to an optimal location of the artifact body (Figure 2.11), another ball is simulated in multiple location choices on the heavy blocks' highest plane.

(a)   (b)

(c)   (d)
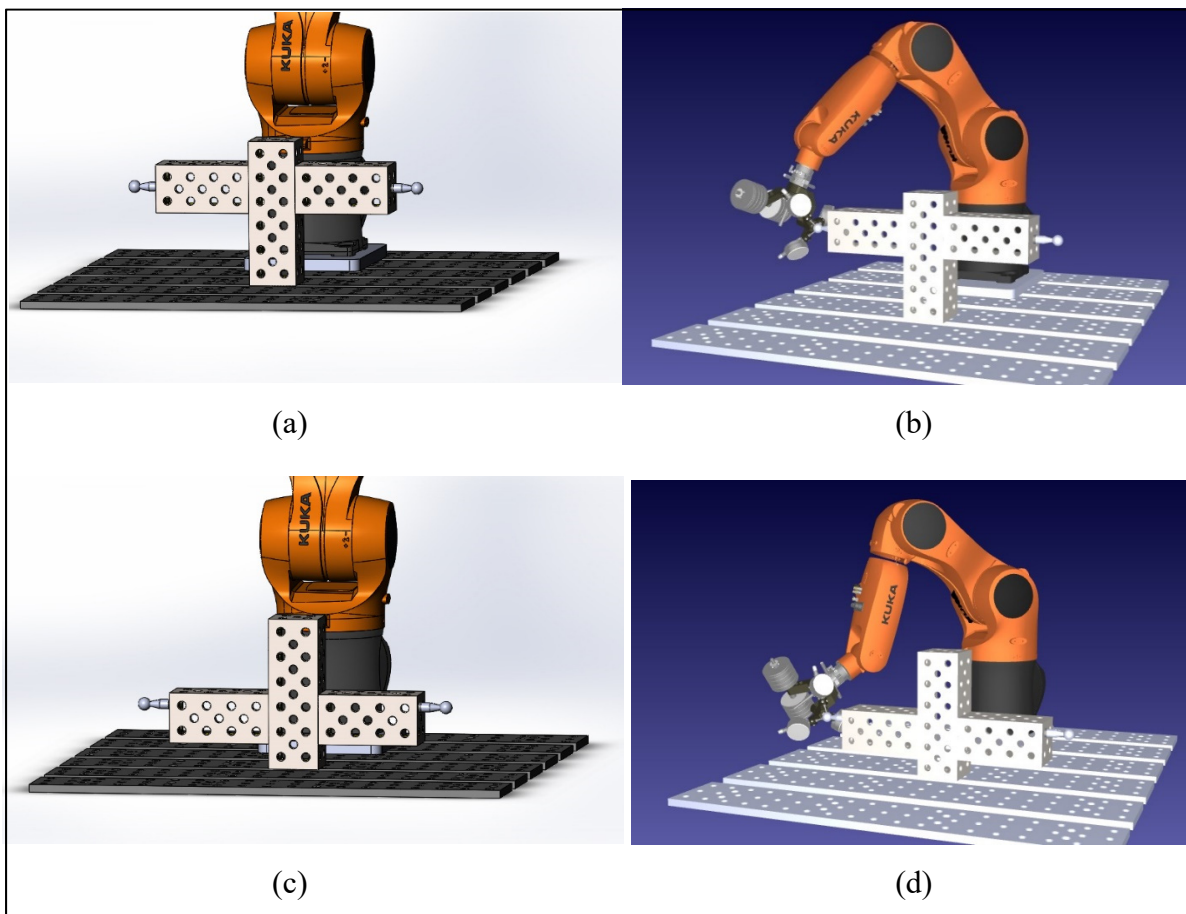
Figure 2.10 Testing and optimizing robot reachability for example designs
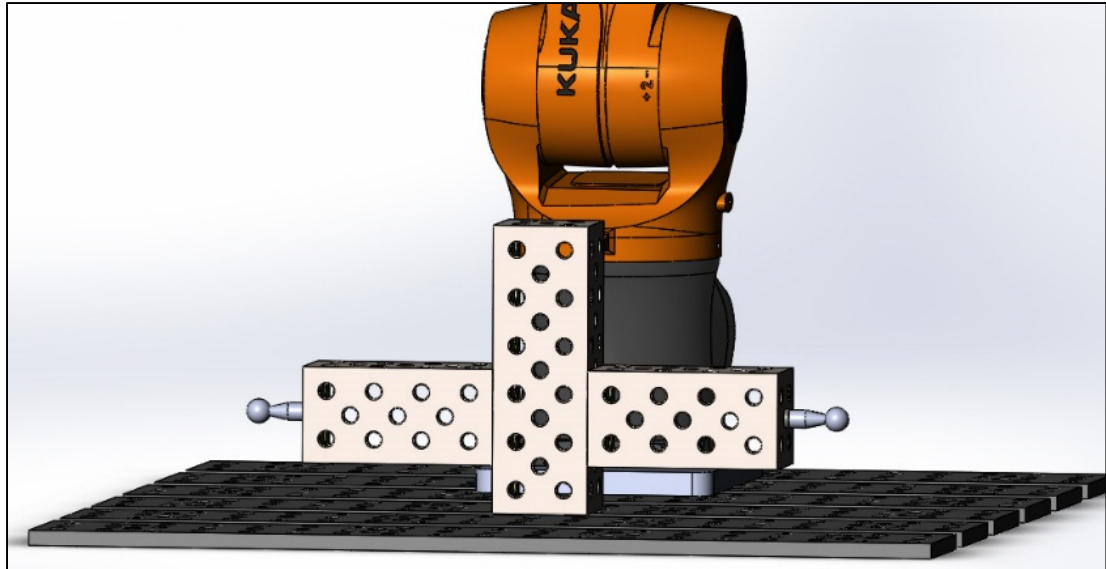
Figure 2.11 Design of the artifact with two datum balls fixed after simulation

This ball placement aims to increase selections of robot elbow movements and to expand the workspace vertically during measurement. Figure 2.12 is some example locations for the third datum ball, and Figure 2.13 illustrates their simulation.

(a)   (b)
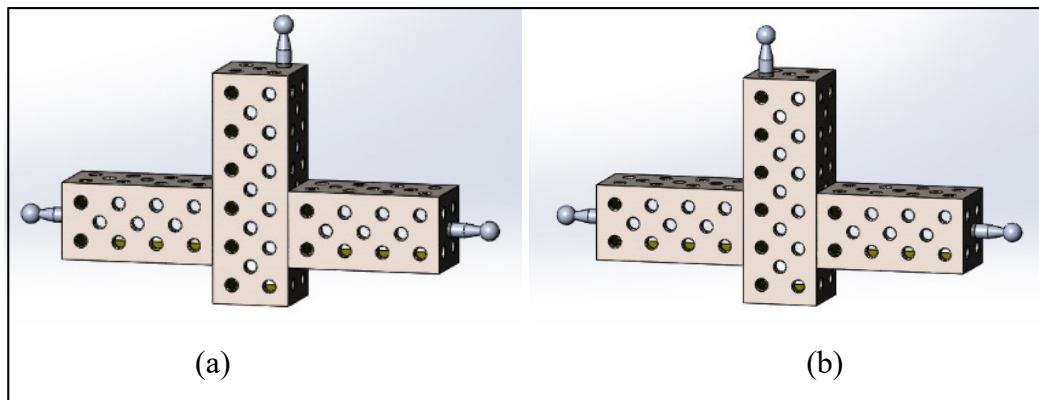
Figure 2.12 Examples of third datum ball implementation to the design

<center>(a)   (b)</center>
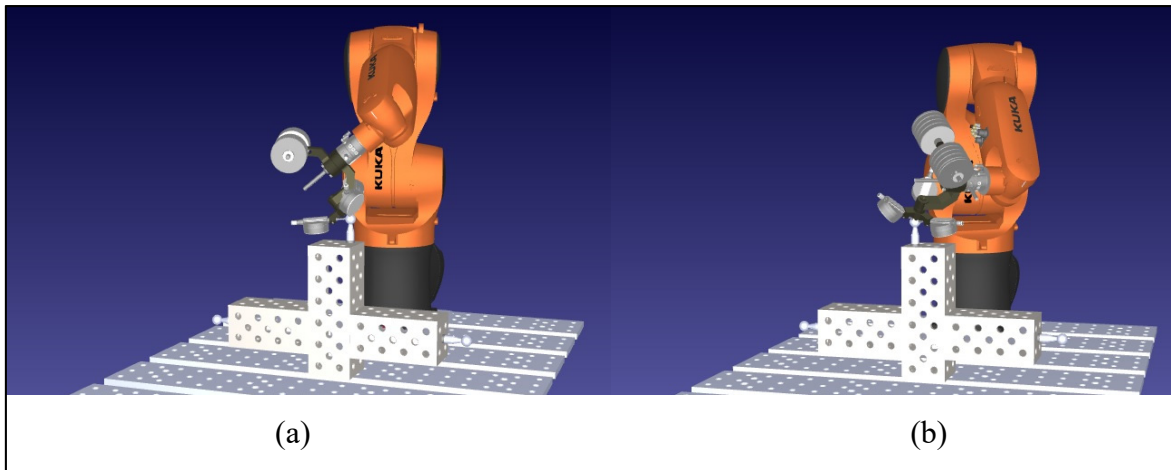
Figure 2.13 Simulations of the third datum ball implemented in RoboDK simulation

After obtaining a total of three balls fixed on the artifact (Figure 2.14), an additional fourth ball is ready for implementation to either of the heavier block sides. Relatively higher possible locations are considered for placement due to the collision possibility with the lighter blocks causing joint set limitations. The fourth ball possible locations are chosen from the opposite plane facing the robot to create multiple datum ball planes on the artifact. Such location examples of the ball are shown in Figure 2.15 and Figure 2.16. This specific plane selection consists of less joint movement restrictions while the robot performs its reach to the desired position.
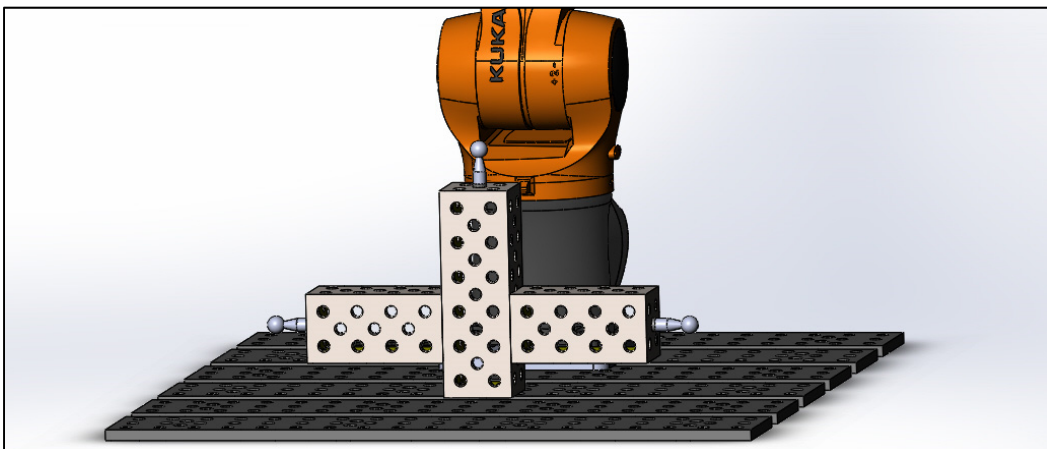
Figure 2.14 Design of the artifact with three datum balls fixed after simulation
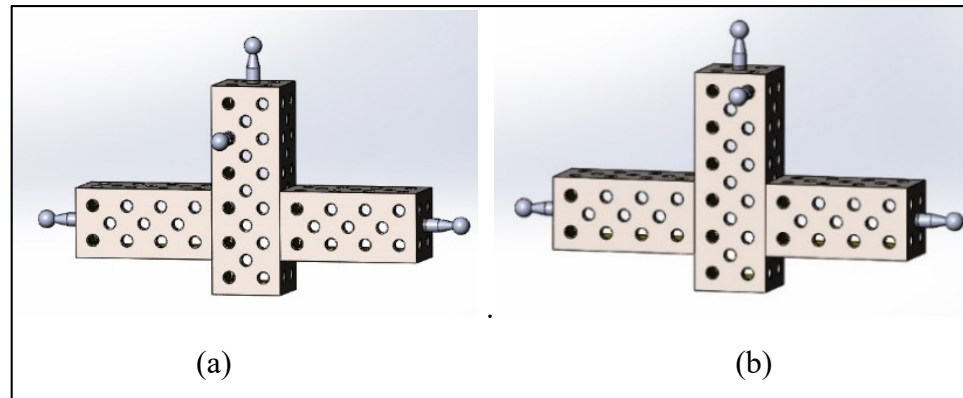
Figure 2.15 Examples of fourth datum ball implementation to the design

Finally, adding a fifth ball location was considered placing symmetrical to the fourth ball plane and facing the robot. However, due to low volume space between the ball center and robot base, elbow, wrist restrictions, joint singularities and tool collisions with the robot occurs often in this condition. Thus, the artifact consists of four datum balls in different planes of the workspace (Figure 2.17).
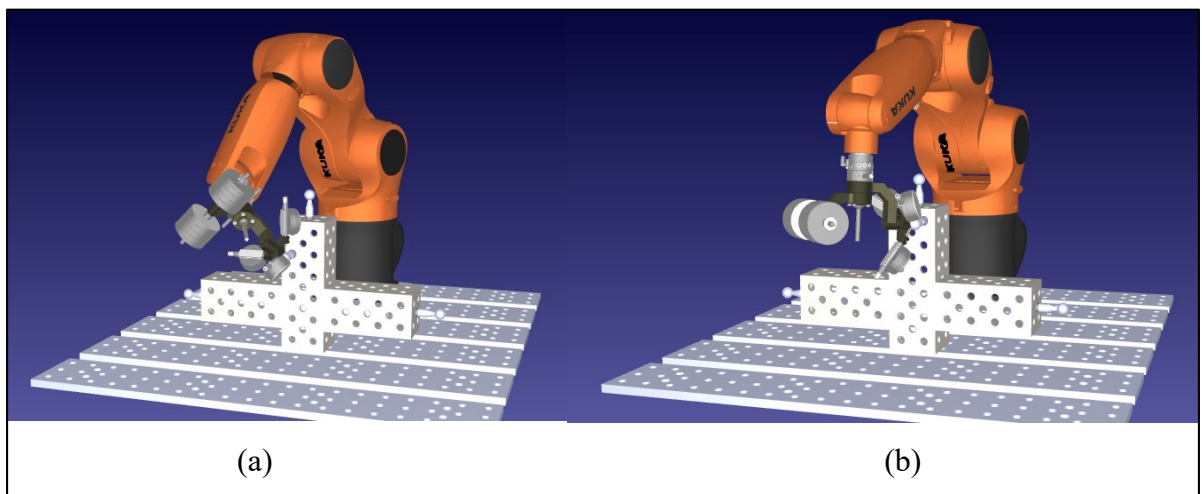
Figure 2.16 Simulations of the fourth datum ball implemented in RoboDK simulation
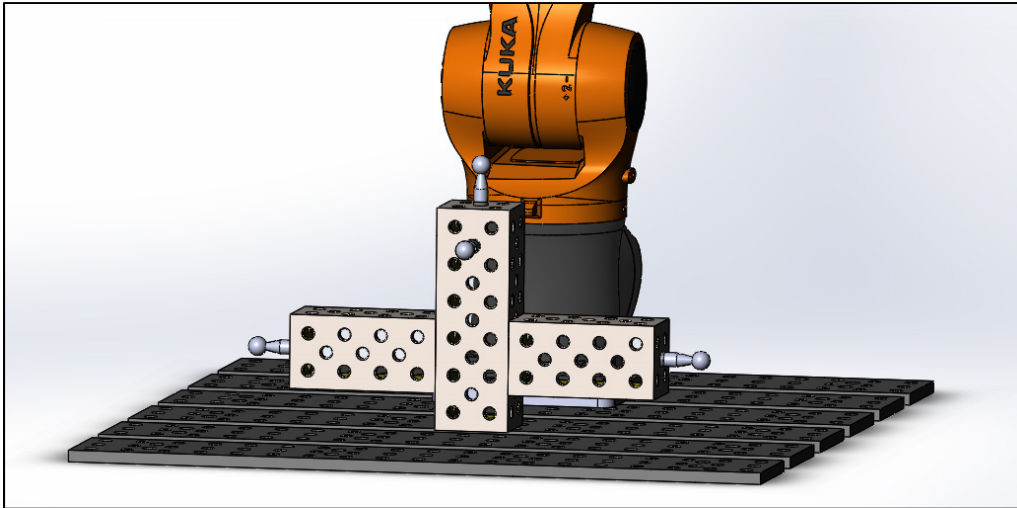
Figure 2.17 Design of the artifact with four datum balls fixed after simulation

2.3.3   Characterization of the artifact

As mentioned in the subsection presenting the artifact components, three magnetic nests for 1.5-in SMRs are also attached to the fixture creating the world reference frame. Their centers define the frame, $x_w y_w z_w$, as shown in Figure 2.18. The locations of the four datum balls with respect to that reference frame are then measured on a Mitutoyo CRYSTA-Apex C 544 CMM (Figure 2.19) and are presented in Table 2.1.
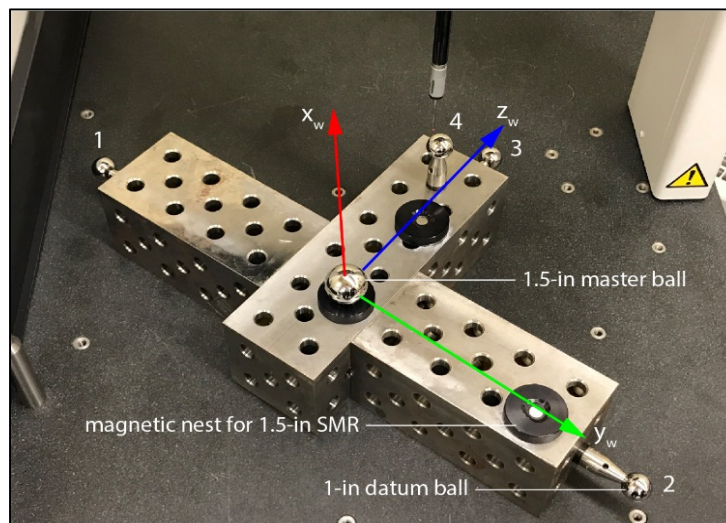
Figure 2.18 The 3D ball artifact during characterization
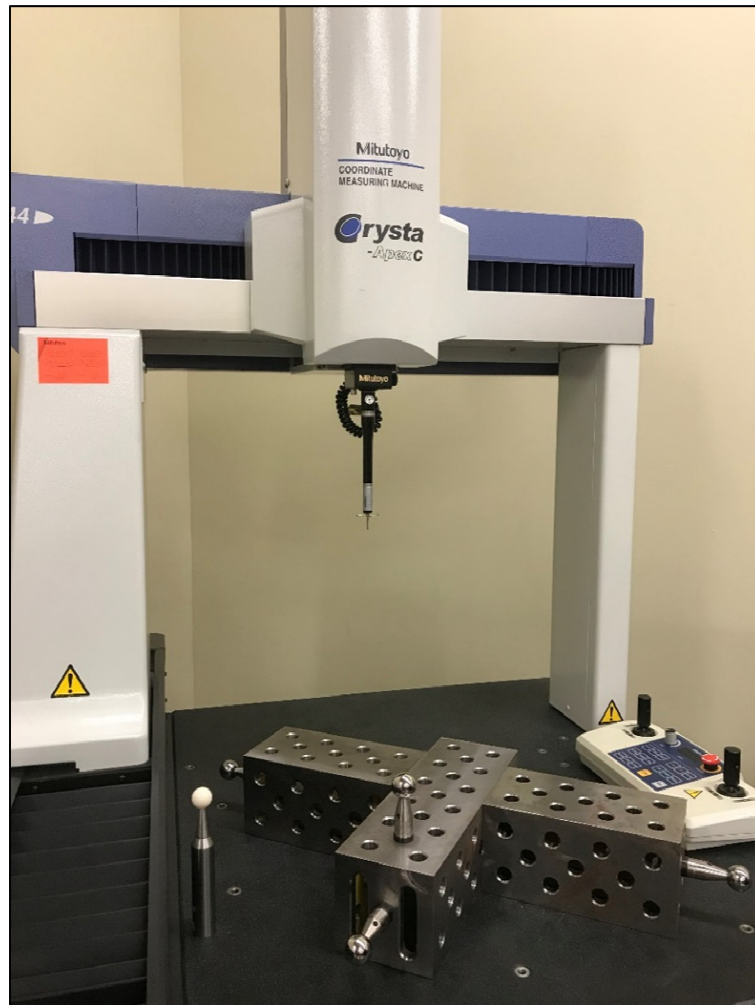
Figure 2.19 The CMM used during artifact measurement

Table 2.1 Positions of the datum balls with respect to the world reference frame

Ball	x [mm]	y [mm]	z [mm]
1	−79.539	−330.141	17.531
2	−79.193	287.805	18.740
3	−79.650	−21.958	276.388
4	26.379	−21.676	170.489

2.4   Communication system

The advantage of the calibration system is that the TriCal device is wireless, thanks to the embedded Bluetooth technology in the Sylvac digital indicators. The Bluetooth signals coming from each indicator are converted to virtual serial ports using Sylvac's V-MUX (Virtual Multiplexer) software in a PC. The PC then communicates with the robot via Ethernet. As described in the following section, the main measurement procedure primarily consists of moving the robot end-effector iteratively until all digital indicators measure a displacement close to zero.

2.5   Measurement procedure

As already mentioned, while presenting the TriCal, the digital indicators are mastered with the 1.5-in master ball, placed manually onto the TriCal nest (Figure 2.3b). Once the master ball in place, each indicator is set to 6.350 mm (Figure 2.3a).

Before the start of the measurement phase, the axes of the cylindrical channels and the center of the master ball while in the trihedral socket are measured on a CMM, all with respect to the tool changer. Then, a tool reference frame is defined such that its center coincides with the center of the master ball and its axes coincide with the axes of the channels. Next, after the artifact measurement on a CMM is performed, it is placed on the robot table to its assigned location. Since the tool reference frame and the datum ball locations with respect to the robot base are known precisely, the TriCal is ready to probe datum balls.

Once the TriCal is physically positioned onto a datum ball (i.e., the contact surfaces of all three digital indicators touch the datum ball), an automated centering sequence is launched, by bringing the robot TCP at the center of the datum ball. Essentially, the measurements from the indicators are read in the PC, and a linear motion command with the respective displacements relative to the tool reference frame is sent to the robot. The sequence is repeated several times until all three indicators read displacements of less than 3 μm. Then, the robot joint encoder values are retrieved in the PC and recorded. The auto-centering sequence lasts 30 seconds on

the average. The robot then backs the TriCal away, moves it to a different approach pose, then brings it to the datum ball with a different orientation. Finally, the auto-centering procedure is launched again. Each of the four datum balls is probed with several different end-effector orientations.

The complete 3D environment was modeled in RoboDK, and the whole measurement procedure was implemented in the same software. Python scripts were written for interfacing with the indicators, for the auto-centering procedure (Figure 2.20), and for the complete measurement sequence. Since RoboDK already comes with the necessary "plugins" to control a KUKA robot over Ethernet, the whole measurement procedure is fully automated and executed from RoboDK simulation, except for the mastering of TriCal.

Algorithm Automated Centering

procedure AUTOCENTERING

    $sr1 \leftarrow$ connection first serial port
    $sr2 \leftarrow$ connection second serial port
    $sr3 \leftarrow$ connection third serial port
    $robot \leftarrow$ robot model
    while contact sphere **do**
        $sr1.flushInput()$ ▷ Remove data from input buffer
        $sr1.flushOutput()$ ▷ Remove data from output buffer
        $sr1.write("\ ".encode())$ ▷ Send request to the indicator along X axis
        $indicator1 \leftarrow$ str(sr1.readline())   ▷ Read the indicator along X

        $sr2.flushInput()$ ▷ Remove data from input buffer
        $sr2.flushOutput()$ ▷ Remove data from output buffer
        $sr2.write("\ ".encode())$ ▷ Send request to the indicator along Y axis
        $indicator2 \leftarrow$ str(sr2.readline())   ▷ Read the indicator along Y

        $sr3.flushInput()$ ▷ Remove data from input buffer
        $sr3.flushOutput()$ ▷ Remove data from output buffer
        $sr3.write("\ ".encode())$ ▷ Send request to the indicator along Z axis
        $indicator3 \leftarrow$ str(sr3.readline())   ▷ Read the indicator along Z

        $refpose \leftarrow$ robot pose   ▷ current robot pose
        $rx \leftarrow$ measurement along indicator1   ▷ Offset on X axis
        $ry \leftarrow$ measurement along indicator2   ▷ Offset on Y axis
        $rz \leftarrow$ measurement along indicator3   ▷ Offset on Z axis
        $targetoffset \leftarrow$ [rx; ry; rz]
        $target \leftarrow$ RelTool(refpose,targetoffset)   ▷ Add offset to pose

        $robot.MoveJ(target)$ ▷ Move robot to target in Joint mode

    end while
end procedure

Figure 2.20 Automated centering algorithm

2.6   Measurement system accuracy

This section presents the accuracy analysis of the complete calibration system and measurement procedure. First, the system components' accuracy is started by observing the sphere balls used in the procedure. The 1-in datum balls and the 1.5-in master ball have the same sphericity tolerance of the value ±1.27 µm, where the BuildingPro welding table and fixtures have precision holes equally spaced with the tolerance of 40 µm. The accuracy of the TriCal digital indicators is 1.8 µm. Finally, the Mitutoyo CRYSTA-Apex C 544 CMM used for characterization of TriCal and the 3D ball artifact has an uncertainty of 1.9 µm.

A measurement analysis took place in the CoRo lab using the TriCal's trihedral socket and digital indicators, along with a 1-in datum ball, a 1.5-in master ball and a robot arm from Mecademic's Meca500 (a very small and highly precise robot arm). The purpose behind this analysis is to prove that when TriCal is centered over a 1-in datum ball such that all three indicators display "0.000", the center of that datum ball is extremely close to the TCP, which is the center of the 1.5-in master ball during mastering. Therefore, this measurement setup seen in Figure 2.21 is performed on a CMM.
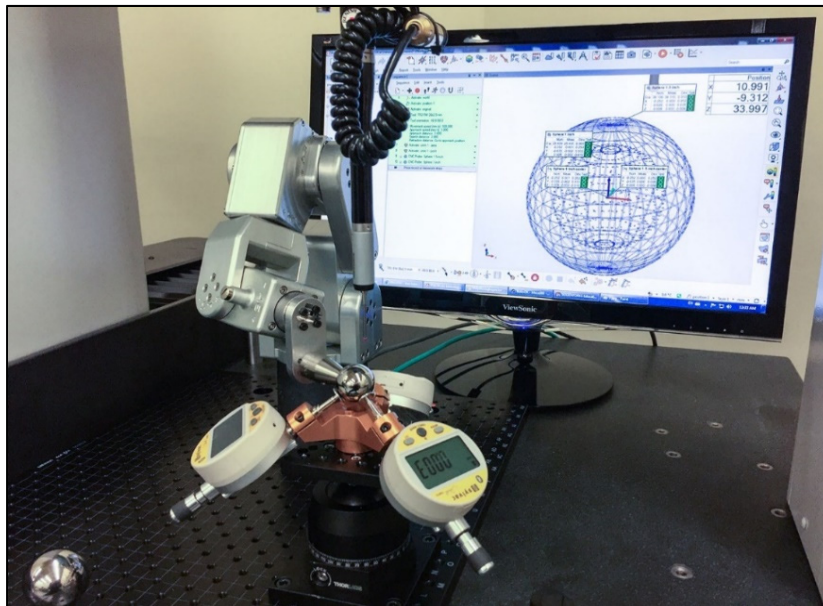
Figure 2.21 Measurement of the TriCal precision

The steps of this procedure start by positioning the 1-5-in master ball in the trihedral socket of TriCal and master all three digital indicators (by setting them to 6.350 mm). Then we measure the position of the master ball with the CMM. This represents the actual TCP of TriCal. A similar setup is used while characterizing the TriCal TCP but with respect to the tool changer of the complete tool assembly. Next, the master ball is removed, and one of the datum balls is mounted via the Meca500 robot. The procedure follows by another auto-centering procedure to move the datum ball until all indicators show a maximum displacement of ±3 μm. We then measured the datum ball with the CMM. The last phase is repeated three times (i.e., measured the datum ball after three auto-centering sequences). The maximum deviation measured between the positions of the datum ball and the master ball position was about 2 μm. This difference validates that the calibration measurement procedure is executed in high accuracy.

CHAPTER 3

ROBOT MODELING

This chapter presents the mathematical model evaluation of the industrial robot used in calibration experimentation. The initial or also called nominal parameters are assigned in this step, followed up with the selection of the error parameters causing absolute position offsets. These error parameters are used and modified in the future step, parameter identification.

Forward kinematics helps us understand the robot geometry and defines the geometric error parameters, while the non-geometric error parameters are found through the dynamic equation calculations. Inverse kinematic equations are mainly used for the 3D ball artifact characterization through inputting possible datum ball locations while generating robot joint configurations. The robot characteristics, along with its kinematic and dynamic equations, are presented in the sections below.

3.1   Description of the robot

In this thesis, the KUKA KR6 R700 sixx robot is used for calibration experimentation shown in Figure 3.1. The six-axis articulated robot weighs a total of 50 kg approximately. The maximum payload capacity is 6 kg, and the robot's position repeatability is 0.03 mm. The robot's reach is 706.7 mm.

Figure 3.1 KUKA KR6 R700 sixx robot (image taken from
https://www.robots.com/robots/kuka-kr-6-r700-sixx)

3.2 Modeling technique and link frame assignments

The Modified Denavit-Hartenberg (MDH) convention is used to describe the robot system's static mathematical model. The frames connecting each link respectively from the robot base to the end-effector are assigned following the procedure presented in Craig (2005). The consecutive parallel axes problem between the 2nd and 3rd axes is dealt by adding an extra parameter β as proposed in Hayati *et al*. (1988). For the dynamic model, through calculating the force and torque applied on the joints, the Newton-Euler algorithm is chosen for the assignment of robot joint stiffness parameters.

The link frames are assigned through the joint pairs from the robot base to the end-effector. The algorithm for assigning these frames (F) is presented below:

1. Identify the joint axis and name it according to the joint number. From 2nd to 5th steps, consecutive joint pairs (axis i and $i + 1$) are considered for assignment;

2. Identify the common perpendicular or point of intersection between axes i and $i + 1$. Assign link frame origin where the common perpendicular meets the ith axis or at the point of intersection between the axes;

3. Assign the $\hat{Z}_i$ axis along the ith joint axis;

4. Assign the $\hat{X}_i$ along the common perpendicular;

5. Assign $\hat{Y}_i$ axis from the right-hand rule;

6. Assign reference frame F_0 through matching F_1 when the 1st joint value is zero. An origin location and $\hat{X}_i$ axis direction is chosen arbitrarily for the F_N (the last frame before the robot tool). Usually, this choice is made upon link parameters getting close to becoming zero after calculation of the equations.

The consecutive parallel axes 2 and 3 are modelled similarly with a small modification, where the $\hat{X}_i$ is assigned normal to the $\hat{Z}_i$ axis plane pointing towards the origin of the $i + 1$ axis.

Figure 3.2 shows the link frames assigned to the robot. Red, blue colored arrows respectively represent coordinate frame axis $\hat{X}, \hat{Z}$. The blue cross symbol represents the $\hat{Z}$ axes pointing towards the inside of the page. (Axes $\hat{Y}$ are not visible as they are normal to the projection plane.)
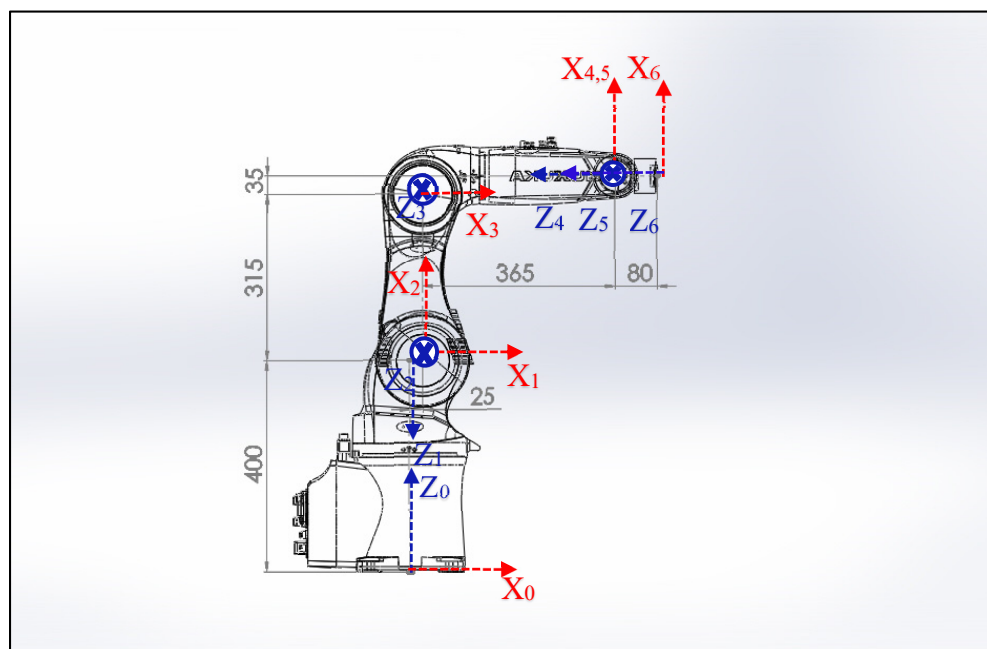
Figure 3.2 Link reference frames shown on the KR6 R700 sixx

3.3 Forward kinematic model

After assigning each frame with a coordinate reference, it is possible to get the forward kinematic model through obtaining the MDH nominal parameters. The definition of these parameters are made through the following certain angle or distance characteristics between reference frames assigned. Four main parameters are described as:

- $\alpha_{i\text{-}1}$ is the angle between $\hat{Z}_{i\text{-}1}$ and $\hat{Z}_i$ measured about $\hat{X}_{i\text{-}1}$
- $a_{i\text{-}1}$ is the distance between $\hat{Z}_{i\text{-}1}$ and $\hat{Z}_i$ measured along $\hat{X}_{i\text{-}1}$
- d_i is the distance between $\hat{X}_{i\text{-}1}$ and $\hat{X}_i$ measured along $\hat{Z}_i$
- θ_i is the angle between $\hat{X}_{i\text{-}1}$ and $\hat{X}_i$ measured about $\hat{Z}_i$

The $\beta_{i\text{-}1}$ represents the consecutive axis parameter. Per Hayati *et al*. (1988), this parameter can be applied to links with parallel or near parallel consecutive joint axes, and they claim that the variations in the link parameters do not correspond to variations in the link coordinate frame. After assigning these parameters and adding the $\beta_{i\text{-}1}$ parameter for the consecutive axis problem, the complete model of the KR6 R700 sixx nominal parameters are presented in Table 3.1 below.

Table 3.1 KR6 R700 sixx nominal parameters

i	$\alpha_{i\text{-}1}$ [°]	$a_{i\text{-}1}$ [mm]	d_i [mm]	θ_i [°]	$\beta_{i\text{-}1}$ [°]
1	180	0	−400	θ_1	-
2	90	25	0	θ_2	-
3	0	315	0	$\theta_3 - 90$	0
4	90	35	−365	θ_4	-
5	−90	0	0	θ_5	-
6	90	0	−80	θ_6	-

These parameters are used for the transformations between the link frames obtained through translations and rotations. The transformation matrix for each frame is calculated through:

$$T_i^{i-1}=R_x(\alpha_{i-1})Tr_x(a_{i-1})R_z(\theta_i)Tr_z(d_i) \tag{3.1}$$

The homogenous transformation matrix of the robot can be calculated by multiplying each frame matrix, respectively. The simplified general matrix obtained through transformation calculations are presented as:

$$T_i^{i-1}=\begin{bmatrix} c\theta_i & -s\theta_i & 0 & a_i \\ s\theta_i c\alpha_{i-1} & c\theta_i c\alpha_{i-1} & -s\alpha_{i-1} & -d_i s\alpha_{i-1} \\ s\theta_i s\alpha_{i-1} & c\theta_i s\alpha_{i-1} & c\alpha_{i-1} & d_i c\alpha_{i-1} \\ 0 & 0 & 0 & 1 \end{bmatrix} \tag{3.2}$$

and by adding the parameter representing the consecutive parallel axis, the matrix calculation for this specific frame is presented as:

$$T_i^{i-1}=R_x(\alpha_{i-1})Tr_x(a_{i-1})R_y(\beta_{i-1})R_z(\theta_i)Tr_z(d_i) \tag{3.3}$$

with the end-result matrix looking like:

$$T_i^{i-1}=\begin{bmatrix} c\theta_i c\beta_{i-1} & -s\theta_i c\beta_{i-1} & s\beta_{i-1} & a_i+d_i s\beta_{i-1} \\ s\theta_i c\alpha_{i-1}+c\theta_i s\alpha_{i-1}s\beta_{i-1} & c\theta_i c\alpha_{i-1}-s\theta_i s\alpha_{i-1}s\beta_{i-1} & -c\beta_{i-1}s\alpha_{i-1} & -d_i c\beta_{i-1}s\alpha_{i-1} \\ s\theta_i s\alpha_{i-1}-c\theta_i c\alpha_{i-1}s\beta_{i-1} & c\theta_i s\alpha_{i-1}-s\theta_i c\alpha_{i-1}s\beta_{i-1} & c\beta_{i-1}c\alpha_{i-1} & d_i c\beta_{i-1}c\alpha_{i-1} \\ 0 & 0 & 0 & 1 \end{bmatrix} \tag{3.4}$$

where $c\theta_i = \cos(\theta_i)$ and $s\theta_i = \sin(\theta_i)$, etc.

For a complete forward kinematic model of the robot system, the base and tool frame matrices are calculated with x, y, z position and α, β, γ orientation representations in the $ZY'X''$ Euler angles convention. The robot base frame (F_0) parameters are calculated with respect to the world frame (F_w), and the tool frame (F_T) parameters are defined with respect to the last axis frame (F_6) of the robot, which is the 6th axis in this case. A total number of 12 base and tool parameters are added as nominal parameters to the robot system, and they are presented in Table 3.2 below.

Table 3.2 Base and tool frame parameters

Frame	x [mm]	y [mm]	z [mm]	α [°]	β [°]	γ [°]
F_w	x_0^w	y_0^w	z_0^w	α_0^w	β_0^w	γ_0^w
F_T	x_T^6	y_T^6	z_T^6	α_T^6	β_T^6	γ_T^6

The equation for these frame calculations is shown as:

$$T(\chi)=Tr(x,y,z)R_z(\alpha)R_y(\beta)R_x(\gamma) \tag{3.5}$$

which gives the simplified end-result matrix as:

$$T(\chi)=\begin{bmatrix} c(\alpha)c(\beta) & -s(\alpha)c(\gamma)+c(\alpha)s(\beta)s(\gamma) & s(\alpha)s(\gamma)+c(\alpha)s(\beta)c(\gamma) & x \\ s(\alpha)c(\beta) & c(\alpha)c(\gamma)+s(\alpha)s(\beta)s(\gamma) & -c(\alpha)s(\gamma)+s(\alpha)s(\beta)c(\gamma) & y \\ -s(\beta) & c(\beta)s(\gamma) & c(\beta)c(\gamma) & z \\ 0 & 0 & 0 & 1 \end{bmatrix} \tag{3.6}$$

A total of 37 nominal parameters are found inside the robot model. It is possible to calculate the forward kinematic equations after having the knowledge of these parameters, through giving joint angle configurations as input to the robot model such as:

$$q =[q_1, \quad q_2, \quad \cdots \quad q_6]^T \tag{3.7}$$

$$T_6^0(q)=T_1^0(q_1)T_2^1(q_2)T_3^2(q_3)T_4^3(q_4)T_5^4(q_5)T_6^5(q_6) \tag{3.8}$$

As output, the position and orientation of the robot pose are determined by multiplying the base and tool transformations with the equation obtained in (3.8). The following equation shows the complete kinematic chain of the robot system as:

$$T_T^W(q)=T_0^W T_6^0(q)T_T^6 \tag{3.9}$$

3.4   Inverse kinematic model

The inverse kinematic equations aim to calculate joint configuration sets through inputting robot end-effector poses. These equations are mainly used for generating joint configurations for calibration experimentation, along with the 3D ball artifact characterization through inputting possible datum ball locations from the workspace. A geometric and algebraic analysis takes place while finding joint characteristics, and the calculations start from equalizing the desired pose of the robot to the matrix found in the equation (3.8). The vectors of the desired pose matrix are defined as:

$$T_D = T_6^0 = \begin{bmatrix} n_x & o_x & a_x & p_x \\ n_y & o_y & a_y & p_y \\ n_z & o_z & a_z & p_z \\ 0 & 0 & 0 & 1 \end{bmatrix} \tag{3.10}$$

3.4.1   Finding joint q_1

To find the first joint value of the robot, we start from calculating the fourth frame origin position with respect to the robot base in the following equation:

$$p_4^0 = T_1^0 T_2^1 T_3^2 T_4^3 \begin{bmatrix} 0 \\ 0 \\ 0 \\ 1 \end{bmatrix} = T_D \begin{bmatrix} 0 \\ 0 \\ -d_6 \\ 1 \end{bmatrix} \tag{3.11}$$

where $c_i = \cos(q_i)$ and $s_i = \sin(q_i)$, etc. This corresponds to:

$$\begin{bmatrix} p_{x4} \\ p_{y4} \\ p_{z4} \end{bmatrix} = \begin{bmatrix} c_1(a_2 + a_3 c_2 + d_4 s_{23} + a_4 c_{2-3}) \\ -s_1(a_2 + a_3 c_2 + d_4 s_{23} + a_4 c_{2-3}) \\ d_1 + a_3 s_2 - d_4 c_{2-3} + a_4 s_{23} \end{bmatrix} = \begin{bmatrix} p_x - d_6 a_x \\ p_y - d_6 a_y \\ p_z - d_6 a_z \end{bmatrix} \tag{3.12}$$

in where the case is not leading to alignment singularities, it is possible to find the equations of q_1 now. We obtain these singularities when the $p_x=d_6a_x$ and $p_y=d_6a_y$ equalities occur. The solutions for q_1 are presented as:

$$q_{1,1}=\text{atan2}\left(-p_y+d_6a_y,p_x-d_6a_x\right) \tag{3.13}$$

$$q_{1,2}=\text{atan2}\left(p_y-d_6a_y,-p_x+d_6a_x\right) \tag{3.14}$$

3.4.2 Finding joints q_3 and q_2

After knowing q_1, the next step is finding the joints q_3 and q_2 from the equality obtained while finding the first joint. These equations can be arranged as:

$$c_1p_{x_4}-s_1p_{y_4}-a_2=a_3c_2+d_4s_{23}+a_4c_{2\text{-}3} \tag{3.15}$$

$$p_{z_4}-d_1=a_3s_2-d_4c_{2\text{-}3}+a_4s_{23} \tag{3.16}$$

Next, we take the square of the equations and adding them together gives us:

$$(c_1p_{x_4}-s_1p_{y_4}-a_2)^2+(p_{z_4}-d_1)^2=a_3^2+d_4^2+a_4^2+2a_3d_4s_3+2a_3a_4c_3 \tag{3.17}$$

Through creating a relation between $\cos(q_3)$ and $\sin(q_3)$ such as:

$$A+Bs_3+Cc_3=0 \tag{3.18}$$

three variables are defined based upon the equation (3.18) above:

$$A=(c_1p_{x_4}-s_1p_{y_4}-a_2)^2+(p_{z_4}-d_1)^2-a_3^2-d_4^2-a_4^2 \tag{3.19}$$

$$B = -2a_3 d_4 \tag{3.20}$$

$$C = 2a_3 a_4 \tag{3.21}$$

Since we know that the squared addition of the same sine and cosine joint value corresponds to 1, we can find the solutions for q_3 from:

$$s_3^2 + \left(\frac{A + B s_3}{C} \right)^2 = 1 \tag{3.22}$$

$$s_3^2 \left(1 + \frac{B^2}{C^2} \right) + s_3 \left(\frac{2AB}{C^2} \right) + \left(\frac{A^2}{C^2} \right) - 1 = 0 \tag{3.23}$$

where the roots of the $\sin(q_3)$ become:

$$s_{3_{1,2}} = \left(\frac{-\frac{AB}{C^2} \mp \sqrt{\frac{A^2 B^2}{C^4} - \left(1 + \frac{B^2}{C^2} \right) \left(\frac{A^2}{C^2} - 1 \right)}}{1 + \frac{B^2}{C^2}} \right) \tag{3.24}$$

After obtaining the cosine of the 3rd joint from equation (3.24) as:

$$c_3 = \frac{A + B s_3}{C} \tag{3.25}$$

it is possible to find the solutions for q_3 as presented below:

$$q_{3_{1,2}} = \text{atan2} \left(s_{3_{1,2}}, \frac{A + B s_{3_{1,2}}}{C} \right) \tag{3.26}$$

The joint q_2 is obtained through defining equations from (3.15) and (3.16). Initially we state that:

$$k_1 = c_1 p_{x_4} - s_1 p_{y_4} - a_2 \tag{3.27}$$

$$k_2 = p_{z_4} - d_1 \tag{3.28}$$

Next, the equations are ordered in a way to obtain the sine and cosine of q_2 while assuming we have the solution of q_3. The equations and solution of the 2nd joint are presented as:

$$\begin{bmatrix} k_1 & k_2 \\ -k_2 & k_1 \end{bmatrix} \begin{bmatrix} s_2 \\ c_2 \end{bmatrix} = \begin{bmatrix} a_3 - d_4 s_3 + a_4 c_3 \\ a_4 s_3 - d_4 c_3 \end{bmatrix} \tag{3.29}$$

$$q_2 = \text{atan2}(s_2, c_2) \tag{3.30}$$

3.4.3 Finding joints q_4, q_5 and q_6

While finding the solutions of the last three joints, the rotation matrix of the last frame with respect to the fourth frame (R_6^3) is in use. We can express the variables of the matrix as:

$$T_6^3 = T_4^3 T_5^4 T_6^5 = \begin{bmatrix} R_6^3 & p_6^3 \\ 0 \quad 0 \quad 0 & 1 \end{bmatrix} \tag{3.31}$$

$$R_6^3 = \begin{bmatrix} r_{1,1} & r_{1,2} & r_{1,3} \\ r_{2,1} & r_{2,2} & r_{2,3} \\ r_{3,1} & r_{3,2} & r_{3,3} \end{bmatrix} = \begin{bmatrix} c_4 c_5 c_6 - s_4 s_6 & -c_4 c_5 s_6 - s_4 c_6 & c_4 s_5 \\ s_5 c_6 & -s_5 s_6 & -c_5 \\ s_4 c_5 c_6 + c_4 s_6 & -s_6 s_4 c_5 + c_4 c_6 & s_4 s_5 \end{bmatrix} \tag{3.32}$$

The solutions found for q_5 are presented as:

$$q_{5,1} = \text{atan2}\left(\sqrt{1 + r_{2,3}^2}, -r_{2,3}\right) \tag{3.33}$$

$$q_{5,2} = \text{atan2}\left(-\sqrt{1 + r_{2,3}^2}, -r_{2,3}\right) \tag{3.34}$$

By knowing the end-result of the 5th joint, we can find the solutions of q_4 and q_6. The last joints of the robot are found through the following equations:

$$q_4 = \text{atan2}\left(\frac{r_{3,3}}{s_5}, \frac{r_{1,3}}{s_5}\right) \tag{3.35}$$

$$q_6 = \text{atan2}\left(\frac{-r_{2,2}}{s_5}, \frac{r_{2,1}}{s_5}\right) \tag{3.36}$$

3.5   Non-geometric parameters

The non-geometric parameters are found by modeling the gearbox of each joint iteratively to identify the stiffness parameters. External variables such as thermal expansion was not considered, due to its negligible impact on the calibration procedure. The gearbox model equation includes a linear torsional spring coefficient calculated with the external torque applied presented as:

$$\delta\theta_i = c_i\tau_i \tag{3.37}$$

where τ is the torque applied on the ith joint couple, $\delta\theta$ being the angle deviation, and c acts as a spring constant being set to 0 initially added to the nominal parameters. By having six joints, normally the same number of constant coefficients are defined to be the non-geometric parameters. However, in the case of the first axis there is no angular deviation occurring, due to its being parallel with the force of gravity. So, as the first axis constant remaining 0, there are 5 non-geometric parameters defined as an addition to the robot model for identification. The Newton-Euler dynamic equations are used for the applied torque calculations and are presented in the subsection below.

3.5.1   Dynamic modeling with the Newton-Euler approach

Craig (2005) uses the Newton-Euler approach to calculate the dynamic motion trajectories of robot systems by computing force and torque in a set of forward and backward iterations. The algorithm equations are presented as:

From $i = 0$ to 5 the equations look like:

$$\omega_{i+1}^{i+1}=R_i^{i+1}\omega_i^i+\dot{q}_{i+1}\hat{Z}_{i+1}^{j+1}$$

(3.38)

$$\dot{\omega}_{i+1}^{i+1}=R_i^{i+1}\dot{\omega}_i^i+R_i^{i+1}\omega_i^i\times\dot{q}_{i+1}\hat{Z}_{i+1}^{j+1}+\ddot{q}_{i+1}\hat{Z}_{i+1}^{j+1}$$

(3.39)

$$\dot{v}_{i+1}^{i+1}=R_i^{i+1}(\dot{\omega}_i^i\times P_{i+1}^i+\omega_i^i\times(\omega_i^i\times P_{i+1}^i)+\dot{v}_i^i$$

(3.40)

$$\dot{vc}_{i+1}^{i+1}=\dot{\omega}_{i+1}^{i+1}\times Pc_{i+1}^{i+1}+\omega_{i+1}^{i+1}\times(\omega_{i+1}^{i+1}\times Pc_{i+1}^{i+1})+\dot{v}_{i+1}^{i+1}$$

(3.41)

$$F_{i+1}^{i+1}=m_{i+1}\dot{vc}_{i+1}^{i+1}$$

(3.42)

$$N_{i+1}^{i+1}=Ic_{i+1}^{i+1}\dot{\omega}_{i+1}^{i+1}+\omega_{i+1}^{i+1}\times Ic_{i+1}^{i+1}\omega_{i+1}^{i+1}$$

(3.43)

follows with the backward iteration from $i = 6$ to 1 looks like:

$$f_i^i=R_{i+1}^i f_{i+1}^{i+1}+F_i^i$$

(3.44)

$$n_i^i=N_i^i+R_{i+1}^i n_{i+1}^{i+1}+Pc_i^i\times F_i^i+P_{i+1}^i\times R_{i+1}^i f_{i+1}^{i+1}$$

(3.45)

$$\tau_i=n_i^{T^i}\hat{Z}_i^j$$

(3.46)

In this case, to obtain a simpler calculation, the robot is considered in a non-moving static situation through some considerations of the variables used in these equations. First, the gravitational effect is implemented to the equations through:

$$\dot{v}_0^0=[0 \quad 0 \quad G]^T$$

(3.47)

Since there is no movement in the joints, the joint velocity and acceleration are 0 along with the angular velocity and acceleration such as:

$$\dot{q}_{i+1}=\ddot{q}_{i+1}=[0 \quad 0 \quad 0]^T \tag{3.48}$$

$$\omega_i^i=\dot{\omega}_i^i=[0 \quad 0 \quad 0]^T, \ \forall i=[1;6] \tag{3.49}$$

An external force is not applied to the robot end-effector which gives us:

$$f_7^7=[0 \quad 0 \quad 0] \tag{3.50}$$

being the final consideration for equation simplification. The mass and the position center of mass for each joint couple and tool are presented in Table 3.3.

Table 3.3 Mass and position center of mass of the robot

i	m_i [kg]	Pc_i^i		
		x [mm]	y [mm]	z [mm]
1	0	0	0	0
2	10	157.5	0	0
3	0	0	0	0
4	10	0	0	182.5
5	0	0	0	0
6	0	0	0	0
T	6	14.3	33.8	97.443

The final version of the Newton-Euler equations become:
-   from $i = 0$ to 5:

$$\dot{v}_{i+1}^{i+1}=R_i^{i+1}\dot{v}_i^i \tag{3.51}$$

$$\dot{v}c_{i+1}^{i+1} = \dot{v}_{i+1}^{i+1} \tag{3.52}$$

$$F_{i+1}^{i+1} = m_{i+1}\dot{v}c_{i+1}^{i+1} \tag{3.53}$$

- from $i = 6$ to 1:

$$f_i^i = R_{i+1}^i f_{i+1}^{i+1} + F_i^i \tag{3.54}$$

$$n_i^i = N_i^i + R_{i+1}^i n_{i+1}^{i+1} + Pc_i^i \times F_i^i + P_{i+1}^i \times R_{i+1}^i f_{i+1}^{i+1} \tag{3.55}$$

$$\tau_i = n_i^{T^i} \hat{Z}_i^j \tag{3.56}$$

3.6   Addition of the error parameters

A total of 43 parameters are defined inside the complete robot model, where 37 of them being geometric along with 6 non-geometric parameters. Not all the parameters are the error parameters according to some considerations regarding redundancy issues and the precision of the frame. 31 of these parameters (26 geometric and 5 non-geometric) are selected to be the error parameters ready for the identification process. Since we take the base frame into identification, the first link errors ($\delta\alpha_0$, δa_0, δd_1, $\delta\theta_{\mathrm{offs}1}$) are dependent on this frame where we don't consider them. The joint axes 2 and 3 parallel to each other also creates redundancy, which leads us to identify any one of the offset length error parameters (δd_2 removed). Finally, since the tool reference frame is precisely measured on a CMM, we do not take the tool frame parameters into the identification process. The error parameters considered in calibration experimentation are shown respectively in Table 3.4 and Table 3.5.

Table 3.4 Geometric and non-geometric error parameters

i	α_{i-1} [°]	a_{i-1} [mm]	d_i [mm]	θ_i [°]	β_{i-1} [°]
1	α_0	a_0	d_1	$q_1+\theta_{offs,1}$	-
2	$\alpha_1+\delta\alpha_1$	$a_1+\delta a_1$	d_2	$q_2+\theta_{offs,2}+\delta\theta_{offs,2}+c_2\tau_2$	-
3	$\alpha_2+\delta\alpha_2$	$a_2+\delta a_2$	$d_3+\delta d_3$	$q_3+\theta_{offs,3}+\delta\theta_{offs,3}+c_3\tau_3$	$\beta_2+\delta\beta_2$
4	$\alpha_3+\delta\alpha_3$	$a_3+\delta a_3$	$d_4+\delta d_4$	$q_4+\theta_{offs,4}+\delta\theta_{offs,4}+c_4\tau_4$	-
5	$\alpha_4+\delta\alpha_4$	$a_4+\delta a_4$	$d_5+\delta d_5$	$q_5+\theta_{offs,5}+\delta\theta_{offs,5}+c_5\tau_5$	-
6	$\alpha_5+\delta\alpha_5$	$a_5+\delta a_5$	$d_6+\delta d_6$	$q_6+\theta_{offs,6}+\delta\theta_{offs,6}+c_6\tau_6$	-

Table 3.5 Base and tool frame error parameters

Frame	x [mm]	y [mm]	z [mm]	α [°]	β [°]	γ [°]
F_w	$x_0^w+\delta x_0^w$	$y_0^w+\delta y_0^w$	$z_0^w+\delta z_0^w$	$\alpha_0^w+\delta\alpha_0^w$	$\beta_0^w+\delta\beta_0^w$	$\gamma_0^w+\delta\gamma_0^w$
F_T	x_T^6	y_T^6	z_T^6	α_T^6	β_T^6	γ_T^6

CHAPTER 4

GENERATION OF CONFIGURATIONS AND PARAMETER IDENTIFICATION

In this Chapter, the generation of robot joint configurations for calibration experimentation and validation steps are presented according to some certain criteria's in order for a safe and complete measurement procedure. After performing a calibration measurement procedure, the robot's new parameters are identified using an optimization algorithm along with the real-time configuration data used in the measurements. The parameter identification method and the algorithm used for optimal configuration generation are explained step by step in the following sections.

4.1   Generation of configurations

Two different classes of configurations are generated for the robot to perform its tasks. The first generated pool of configurations is regarding the identification process, and the second pool is generated for the validation procedure.

For the identification process, since the datum ball positions are known with respect to the robot base (covered in Chapter 2), it is possible to find joint configurations physically probing the datum balls desired positions from the inverse kinematic calculations of the robot model. The detailed calculations of the inverse kinematic equations were presented in the previous Chapter regarding the complete robot model (Chapter 3). Since the desire is to obtain a fully completed and safe measurement procedure, the collision map of the pool configurations is observed through RoboDK. The configurations causing a collision with any component of the system are eliminated from the pool. In Figures 4.1 and 4.2, two different offline collision cases are compared and illustrated with a non-colliding case.
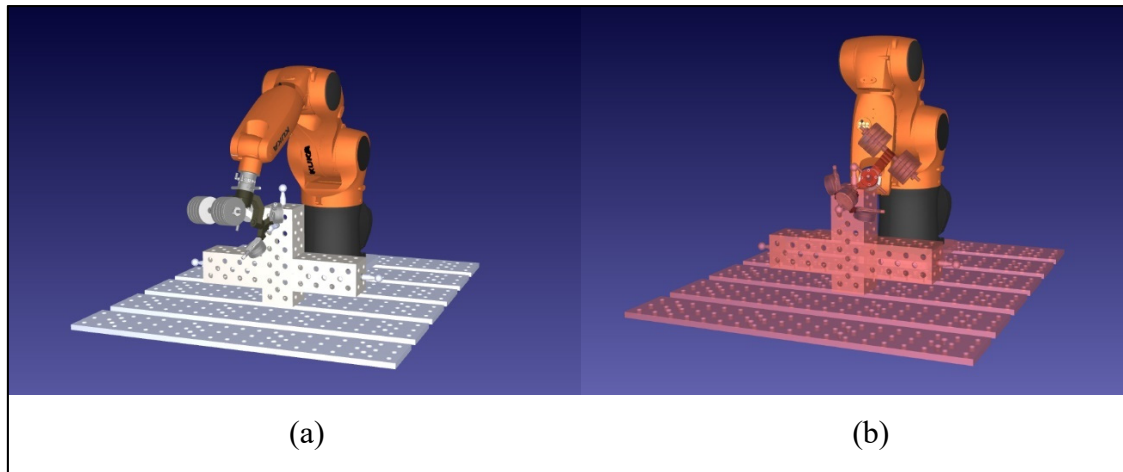
Figure 4.1 Comparison of an offline collision occurring in the tool level
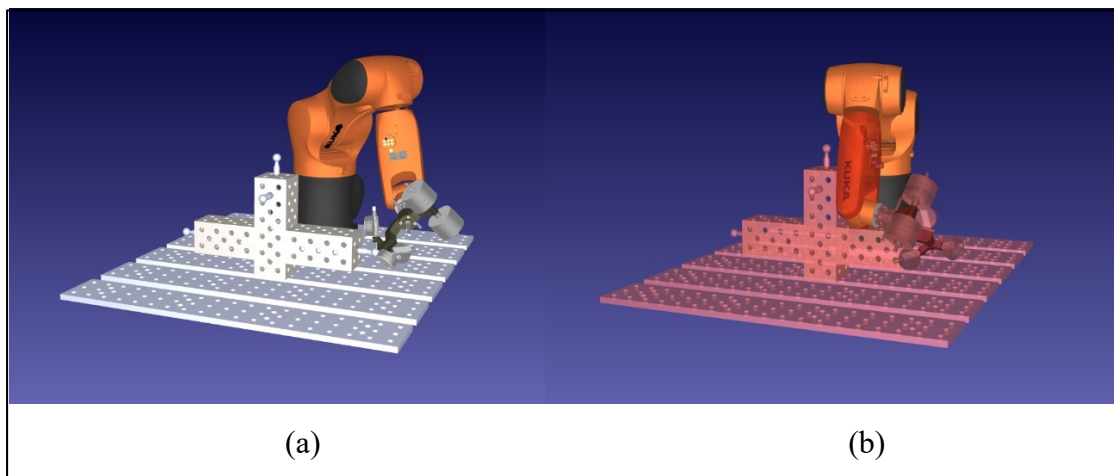
Figure 4.2 Comparison of an offline collision occurring in one of the robot links

As for the validation configurations, they are generated accordant to a laser tracker measurement procedure in the robot workspace. This means that there are not fixed physical positions in the workspace to take a reference. Instead, random joint configurations are distributed to the whole robot workspace with the condition that the SMR eye is facing towards the laser tracker for a clear visual (recalling that the SMR can be attached to the TriCal through a magnet). Since there is a removal of the 3D ball artifact just before the validation measurements, the only collision map encountered in the validation pool was colliding with the robot table (a collision comparison illustrated in Figure 4.4). To simplify this step, a new temporary tool frame is initialized with extra orientations applied to the existing TriCal TCP

translation data. Thus, one of the tool coordinate vectors $(\hat{Y}_T)$ is pointed towards the laser tracker, as seen in Figure 4.3 below.

Figure 4.3 The temporary tool frame for validation configurations
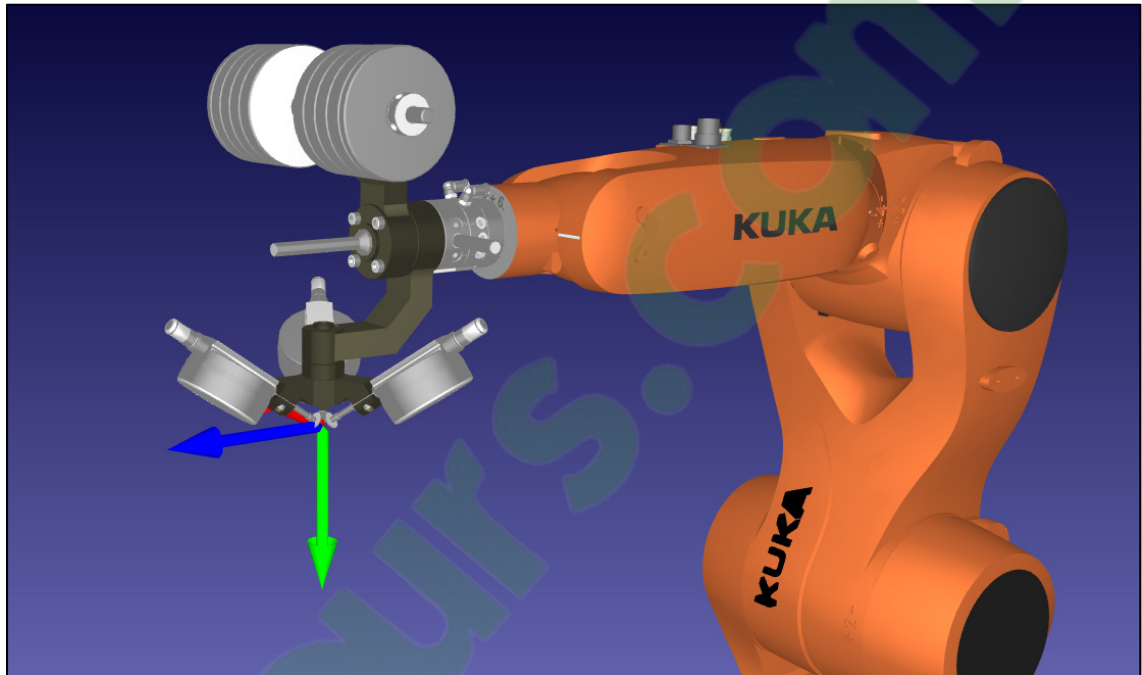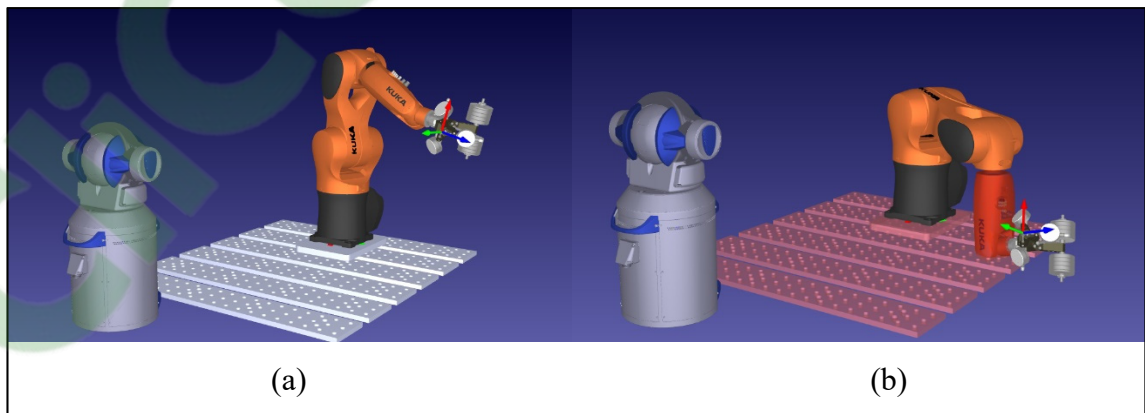

| (a) | (b) |

Figure 4.4 Comparison of an offline collision occurring in one of the robot links

4.2   Linear least-squares optimization

The identification method plays a vital role for a closer parameter estimation of the real robot. One of the most common methods used in robot parameter identification is the least-squares

method, and in our case, it is also used in this thesis by linearizing the non-linear robot equations around the initial parameters. As the end-result, the new robot parameters should give us a better robot end-effector positioning in terms of accuracy. The detailed description of this method is presented in the following paragraphs.

Our position error model uses equations for n measurements, which is calculated with the end effector position data obtained by the real robot measurements and the forward kinematic solutions giving the desired estimated values per robot pose:

$$\Delta X^n = x^n_{measured} - x^n_{est} \tag{4.1}$$

The initial forward kinematic representation of finding the estimated end-effector position is represented as:

$$x_{est} = \begin{bmatrix} x^W_T \\ y^W_T \\ z^W_T \end{bmatrix} = f(\rho, q, \tau) \tag{4.2}$$

where the initial nominal parameters include:

$$\rho = [\alpha^T, a^T, d^T, \theta^T_{offs}, \beta_2, F^T_T, F^T_W, c^T]^T \tag{4.3}$$

ρ as the constant parameters, and the q, τ parameters are included representing the variable parameters. It is enough to initialize the estimated end-effector position with the translation vector considering the tool's orientation not being included into calibration.

Since our position error model in n measurements is desired to converge to zero as:

$$x^n_{measured} - f(\rho, q^n, \tau^n) \approx 0 \tag{4.4}$$

the non-linear equations can be linearized through differentiating the desired (estimated) end-effector position equations around the nominal parameters such as:

$$\Delta X^n = \begin{bmatrix} x^n_{measured} - x^n_{est} \\ y^n_{measured} - y^n_{est} \\ z^n_{measured} - z^n_{est} \end{bmatrix} = J^n \Delta\rho \tag{4.5}$$

where J^n is the identification Jacobian matrix and its matrix elements differentiation can be represented as:

$$J^n = \frac{\partial f(\rho, q^n, \tau^n)}{\partial\rho} \tag{4.6}$$

$$J = \begin{bmatrix} \frac{\partial f_1}{\partial\rho_1} & \frac{\partial f_1}{\partial\rho_2} & \frac{\partial f_1}{\partial\rho_3} & \cdots & \frac{\partial f_1}{\partial\rho_m} \\ \frac{\partial f_2}{\partial\rho_1} & \frac{\partial f_2}{\partial\rho_2} & \frac{\partial f_2}{\partial\rho_3} & \cdots & \frac{\partial f_2}{\partial\rho_m} \\ \frac{\partial f_3}{\partial\rho_1} & \frac{\partial f_3}{\partial\rho_2} & \frac{\partial f_3}{\partial\rho_3} & \cdots & \frac{\partial f_3}{\partial\rho_m} \end{bmatrix} \in R^{3\times m} \tag{4.7}$$

m is the number of the parameter vector $\rho=[\rho_1, \quad \rho_2, \quad \cdots \quad \rho_m]^T$ (in our case 31 parameters ready for identification). The identification Jacobian is a $3n\times m$ matrix, and by multiplying it with the parameter vector with the size of $m\times1$, the position error vector ΔX is obtained in the $3n\times1$ dimension:

$$\Delta X_{(3n\times1)} = J_{(3n\times m)}\Delta\rho_{(m\times1)} \tag{4.8}$$

Since the objective in the least-squares method is to minimize the sum of squared error value differences between the model values and the measured values such as:

$$min\ (\Delta X - J\Delta\rho)^T(\Delta X - J\Delta\rho) \tag{4.9}$$

It is possible to arrange the equations in a manner where the parameter difference $\Delta\rho$ is the output of the equations since we know the position error vector ΔX, and the Jacobian matrix elements from the position measurements compared to the model. The Jacobian matrix is inverted with Moore-Penrose inverse ($^+$) and getting the final equation looks like:

$$J^T J \Delta\rho = J^T \Delta X \tag{4.10}$$

$$\Delta\rho = (J^T J)^{-1} J^T \Delta X \tag{4.11}$$

$$\Delta\rho = J^+ \Delta X \tag{4.12}$$

4.3   Parameter identification algorithm

The iterative algorithm of finding the new identified robot parameters is presented in this section to get the best optimal parameter vector. Kaveh *et al.* (2016) uses the same iteration to find a good estimation in their robot parameters. The procedure is as follows:

1. Initialize the vector ρ to the nominal parameter values ($\rho = \rho_{nom}$);
2. Calculate the identification Jacobian matrix J and the estimated position of the end-effector x_{est}^n vector using the initialized ρ vector, and the joint q^n and torque τ^n vectors for all the n robot configurations;
3. Calculate the position error vector ΔX^n through the difference between the estimated end-effector position vector and the measured end-effector position vector such as $\Delta X^n = x_{measured}^n - x_{est}^n$;
4. Invert the matrix J to its pseudo-inverse and leave the parameter vector ρ as the output in the newly formed equation: $\Delta\rho = J^+ \Delta X$;
5. Calculate the $\Delta\rho$ from the formed equation;
6. Add the values $\Delta\rho$ to the initial values of the parameter vector ρ, such as: $\rho = \rho + \Delta\rho$;
7. Follow the steps (2) to (6) and repeat them until the absolute value of the position errors converges to an arbitrary value;
8. The end result ρ is the final assumption for the identified robot parameters.

4.4 Observability analysis

An observability estimation is made in order to find the optimal set of generated joint angle configurations. Optimal robot calibration poses are critical for a better measurement procedure leading to a better observation of identifying the new robot parameters. As mentioned in the first Chapter of the thesis, Joubair *et al.* (2013) reviewed all existing five observability indices O_1, O_2, O_3, O_4, O_5. Since we include the non-kinematic parameter identification into calibration, the observability index O_1 is chosen as the best index to use for a complete model. The equation of the chosen index is presented with the equation below:

$$O_1 = \frac{\sqrt[m]{\sigma_1 \sigma_2 \ldots \sigma_m}}{\sqrt{n}} \tag{4.13}$$

where n is the number of joint sets used in measurements, m is the number of calibration parameters, σ are the singular values taken from the Jacobian matrix. The singular value decomposition (SVD) is defined as:

$$J = U \sum V^* \tag{4.14}$$

where J represents the identification Jacobian matrix, U being a unitary matrix with the size of $n \times n$, V^* being the adjoint of a unitary matrix V with the size of $m \times m$. $\sum$ is a diagonal $n \times m$ matrix where the singular values of the J matrix is stored as:

$$\sum = \begin{bmatrix} \sigma_1 & 0 & \ldots & 0 \\ 0 & \sigma_2 & \ddots & \vdots \\ \vdots & \ddots & \ddots & 0 \\ 0 & \ldots & 0 & \sigma_m \end{bmatrix} \tag{4.15}$$

The output joint angles are chosen using the DETMAX algorithm presented by Mitchell (1974). The algorithm consists of rearranging an initial set of n joint angles by adding from and extracting to an N configuration pool, until getting the best observability index inside the n joint set. The detailed methodology of this iterative algorithm is as follows:

1. Generate a large pool of N joint configurations;

2. Calculate the identification Jacobian matrix J for each existing joint configuration;

3. Define an initial set of n joint configurations out of the N configuration pool. This joint set is initialized as Ω_0 and, the final joint set found from this iteration will be Ω_f;

4. One joint configuration from the pool configurations different from the initially chosen ones is selected and added to the Ω. All the rest of the $N-n$ configurations execute this same step apart from each other. The observability index is calculated for each added configuration, and the configuration returning the largest index is kept in the Ω, forming a set of $n+1$ configurations;

5. One joint configuration is removed from the Ω set, which contained $n+1$ configurations after the addition step. The observability index is calculated each time a configuration is removed for all the set elements remaining. Lastly the configuration returning the lowest index is removed from the Ω, forming back to a set of n configurations.

The configurations addition, removal steps are carried on until the added and removed configuration becomes the same in an iteration.

CHAPTER 5

CALIBRATION EXPERIMENTATION, VALIDATION AND RESULTS

This chapter presents an explanation of the new calibration system experimentation, its validation step and the generated results from this procedure. First, the new calibration system experiments are recapped and explained in detail, along with the presentation of the identified robot parameters. Next, the validation procedure is executed. Finally, the validation results are presented, followed by a comparison analysis of the calibration performance for the new system versus a traditional laser tracker. The steps presented above are all executed on the KUKA KR6 R700 sixx robot.

5.1 Experimentation with the new calibration system

Before the calibration experimental setup to take place, the components of the new system are integrated into the robot cell. The robot location is fixed on a precise table through a base plate, followed by the implementation of the characterized tool and fixture components (mentioned in Chapter 2). Next, the 3D ball artifact is fixed to the location assigned from the simulation tests executed in RoboDK (mentioned in Chapter 2). The joint configuration pool is sorted using the observability index algorithm. A total of 80 optimal joint configurations (20 for each datum ball) are selected for the real-time measurement procedure. Since physical contacts exist in the system procedure, the robot program is executed in a constant speed in order to avoid future physical inaccuracies. Figure 5.1 illustrates the experimental measurement procedure with TriCal probing one of the 3D ball artifact datum balls in an optimal configuration.
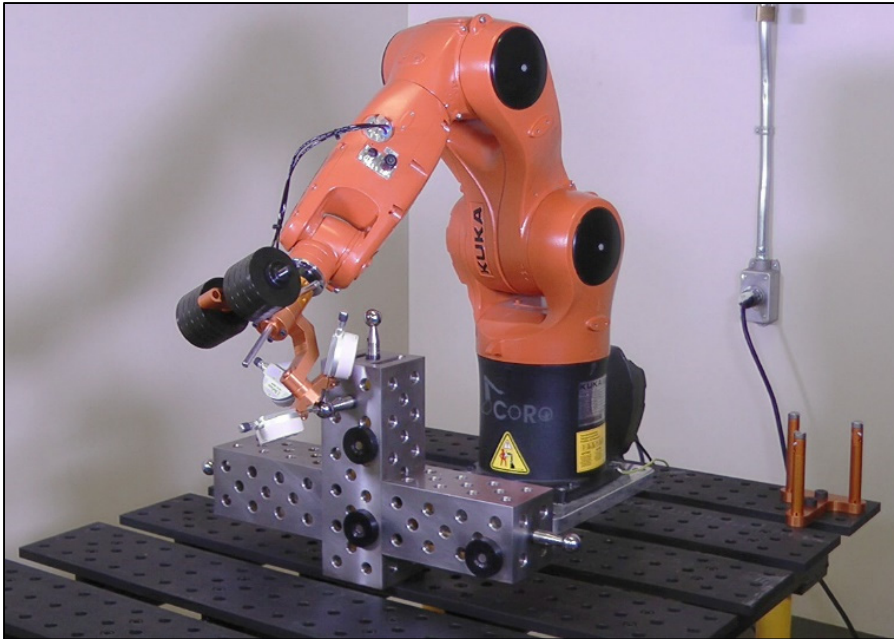
Figure 5.1 TriCal and the 3D ball artifact fixed during measurements

5.2   Validation step using a laser tracker

Validation is performed using a FARO laser tracker once the new robot parameters are identified. The laser tracker is distanced approximately 0.9 m away from the artifact and facing towards the robot. The validation setup is illustrated in Figure 5.2.
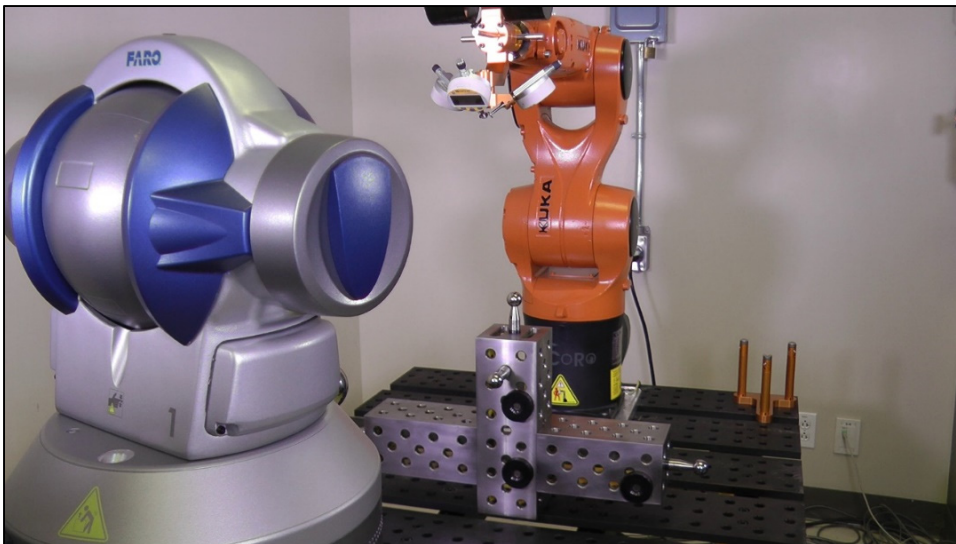

Figure 5.2 FARO laser tracker facing towards the robot during validation

Firstly, the world reference frame with respect to the laser tracker frame is obtained by measuring the three magnetic nests' positions on the 3D ball artifact. To get a proper frame transformation, this step can be executed through dragging the SMR from the laser tracker base towards the 3D ball artifact and recording every measurement once the SMR is fixed to the magnet and visible from the laser tracker. Then, the artifact is removed, and an SMR is positioned in the trihedral socket of TriCal with the help of a rare-Earth magnet (this step was mentioned in Chapter 2). Recall that the center of the SMR corresponds exactly to the robot TCP.

The robot is then sent to 500 random joint sets, with the only constraints of avoiding collisions and having the SMR face the laser tracker (as mentioned in Chapter 4). The measurement procedure and some example measured laser tracker joint poses are shown in Figure 5.3.
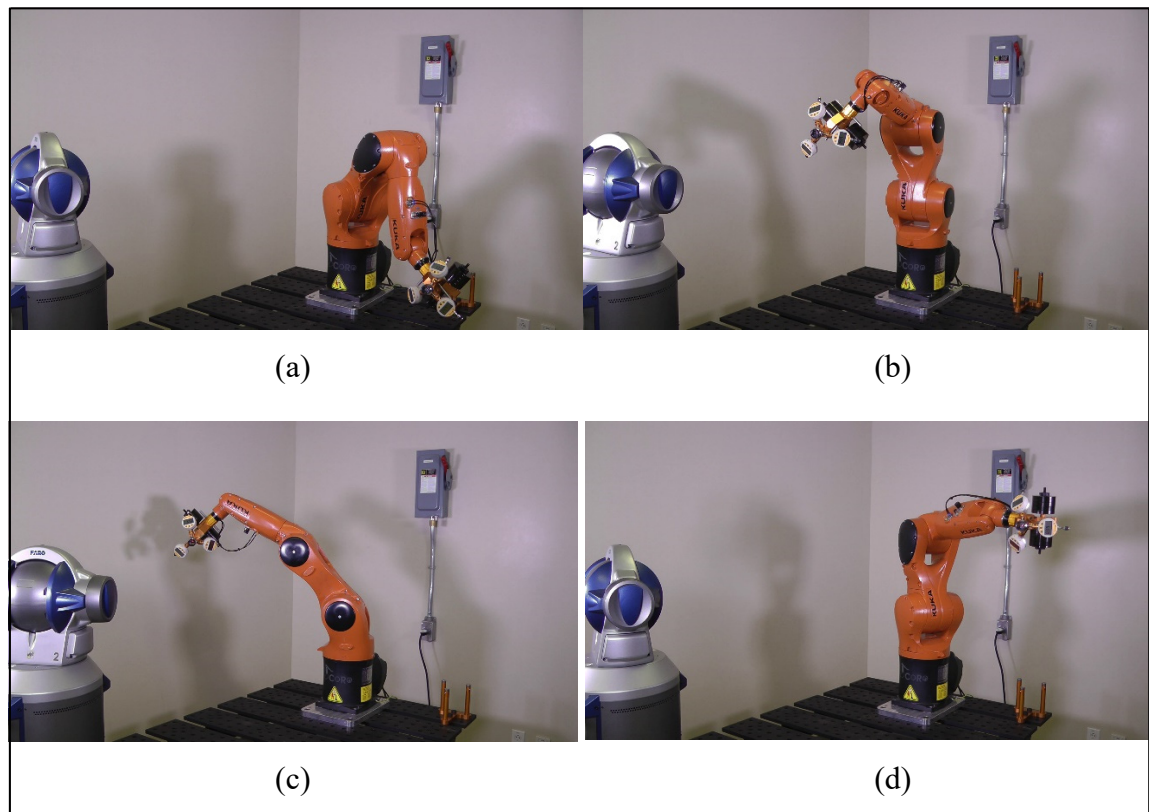

Figure 5.3 Laser tracker poses measured in the whole workspace

5.3   Experimental results

The robot parameter identification is executed after the measurements using the calibration system, and these new parameters are presented in Table 5.1. Then the position errors after calibration (i.e., after using the identified parameters in Table 6) and measured with the laser tracker in 500 poses are presented in Figure 5.4, along with Table 5.2 comparing the position errors before and after calibration.

Table 5.1 Comparison of nominal and identified robot parameters

Parameters	Nominal	Identified
x_0^w [mm]	−536.320	−538.014
y_0^w [mm]	−21.901	−23.563
z_0^w [mm]	−58.349	−58.157
α_0^w [°]	0.000	0.254
β_0^w [°]	0.000	0.014
γ_0^w [°]	0.000	0.172
α_1 [°]	90.000	90.005
α_2 [°]	0.000	−0.015
α_3 [°]	90.000	89.999
α_4 [°]	−90.000	−89.895
α_5 [°]	90.000	89.983
a_1 [mm]	25.000	25.243
a_2 [mm]	315.000	315.16
a_3 [mm]	35.000	35.106
a_4 [mm]	0.000	0.075
a_5 [mm]	0.000	0.032
d_3 [mm]	0.000	0.067
d_4 [mm]	−365.000	−365.34
d_5 [mm]	0.000	0.001

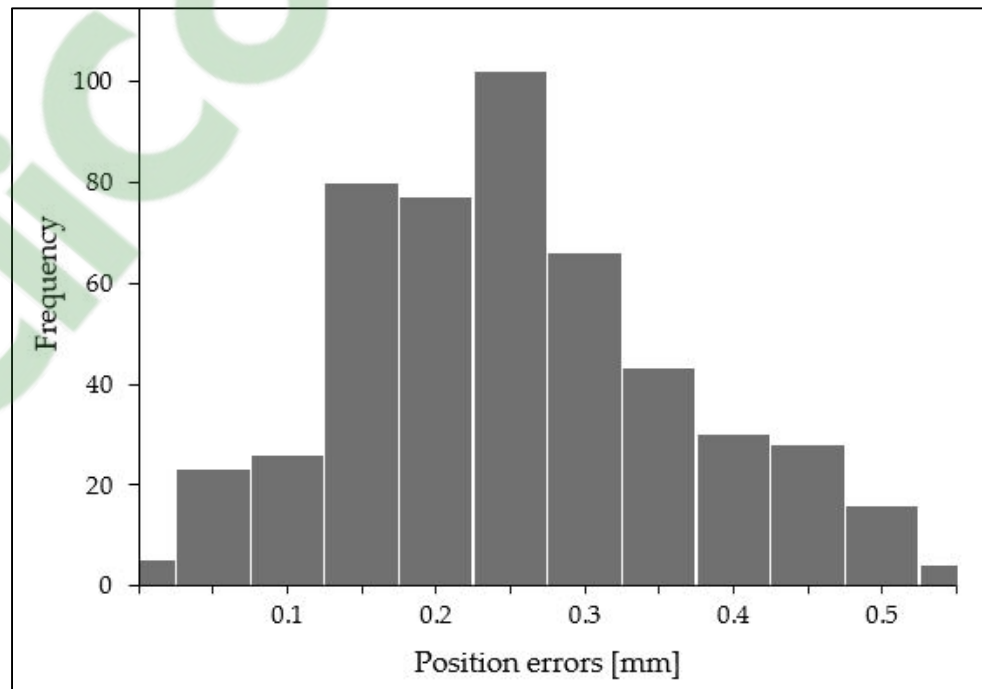| Parameters	Nominal	Identified
d_6 [mm]	−80.000	−80.279
θ_2 [°]	0.000	0.026
θ_3 [°]	−90.000	−89.956
θ_4 [°]	0.000	0.007
θ_5 [°]	0.000	0.015
θ_6 [°]	0.000	0.012
β_2[°]	0.000	−0.005
c_2 [°/Nm×10^{-3}]	0.000	2.987
c_3 [°/Nm×10^{-3}]	0.000	−3.238
c_4 [°/Nm×10^{-3}]	0.000	−8.723
c_5 [°/Nm×10^{-3}]	0.000	−25.489
c_6 [°/Nm×10^{-3}]	0.000	−28.161

Figure 5.4 Histogram of position errors after calibration

Table 5.2 Summary of position errors before and after calibration

Parameters	Mean [mm]	Maximum [mm]	StdDev [mm]
Nominal	2.423	4.235	0.828
Identified	0.326	0.624	0.107

5.4 Comparison between calibration measurement methods

Finally, to validate our hypothesis, the efficiency comparison of the TriCal measurement to that of the laser tracker, when it comes to robot calibration, an identification using measurements taken only with a laser tracker is performed. Specifically, 80 measurements are taken throughout the robot's workspace, selected using the observability analysis described in Chapter 4. Then, the accuracy after calibration was measured in the same 500 poses used in the case of TriCal. The maximum weight payload of the robot (6 kg) is once again implemented for a viable comparison between methods. As expected, the laser tracker leads to slightly better results because the measurements used for identification are more evenly distributed throughout the workspace of the robot. However, it is safe to say that the cost-efficiency using the TriCal is much better than the laser tracker, considering the TriCal and 3D ball artifact components adding up to an approximate price of 5,000 US$, and on the other hand, the laser tracker having a minimum price close to 100,000 US$. The results are shown in Table 5.3.

Table 5.3 Comparison of position errors after calibration with TriCal and laser tracker

Method	Mean [mm]	Maximum [mm]	StdDev [mm]	Cost (US$)
TriCal	0.326	0.624	0.107	≈5,000
Laser Tracker	0.231	0.539	0.087	>100,000

CONCLUSION AND RECOMMENDATIONS

A practical procedure for on-site robot calibration based on a novel wireless 3D measurement device and an artifact fixture was presented in this thesis. The proposed calibration procedure can be summarized step by step as:

1. Attach the 3D ball artifact, preliminarily inspected on a CMM, to the robot's base support, in a precisely known location;
2. Attach the TriCal, preliminarily adjusted with the desired total weight and inspected on a CMM, to the flange of the industrial robot;
3. Start the robot in manual mode, reorient TriCal upwards and then manually master the three digital indicators;
4. Switch the robot to automatic mode and run RoboDK on PC connected to the robot;
5. Execute the probing for each of the four datum balls with 20 different orientations, preliminarily determined through observability analyses. Each probing is based on the auto-centering procedure. Once all 80 joint targets are recorded, identify the 31 robot parameters;
6. Once these 31 robot parameters identified, use RoboDK to calculate so-called fake targets for each new desired end-effector pose.

The calibration system containing the TriCal and the 3D ball artifact was presented in Chapter 2 with their detailed characterization. The method was tested on a KUKA KR6 R700 sixx industrial robot and its modeling using the Modified Denavit-Hartenberg convention with an extra parameter addition along with the identification of the non-geometric stiffness parameters were explained in Chapter 3. The joint configuration pool decision for the experimentation setup, the criteria while choosing optimal configurations from this pool and the parameter identification method using the least-squares method were explained in Chapter 4. Finally, the experimentation results and a performance comparison with a traditional laser tracker measurement method was presented in Chapter 5. The measurements for identification

and the measurements for validation with FARO laser tracker are demonstrated in a video in Appendix I of this thesis.

The calibration yielded the mean position error value to 0.326 mm from 2.423 mm, the maximum position error to 0.624 mm from 4.235 mm and the standard deviation to 0.107 from 0.828 mm. It was found that the efficiency of the new method is close to that of a laser tracker when it comes to calibrating a small industrial robot. Nevertheless, the new device and the 3D ball artifact (≈US$ 5,000) are several times less expensive than a traditional laser tracker (>$US 100,000). Several units of the TriCal have been manufactured, and a few have already been sold to robot manufacturer and university researchers (as seen in Appendix II).

To further improve this method's efficiency, even though the TriCal contains a compact and portable design, more research is needed on the design of the 3D ball artifact. A wider distribution of the datum balls is needed, and the artifact could be more portable by decreasing the mass while maintaining stability at the same time.

APPENDIX I

**CALIBRATION PROCEDURE AND VALIDATION STEP INTRODUCED
IN A SHORT VIDEO**
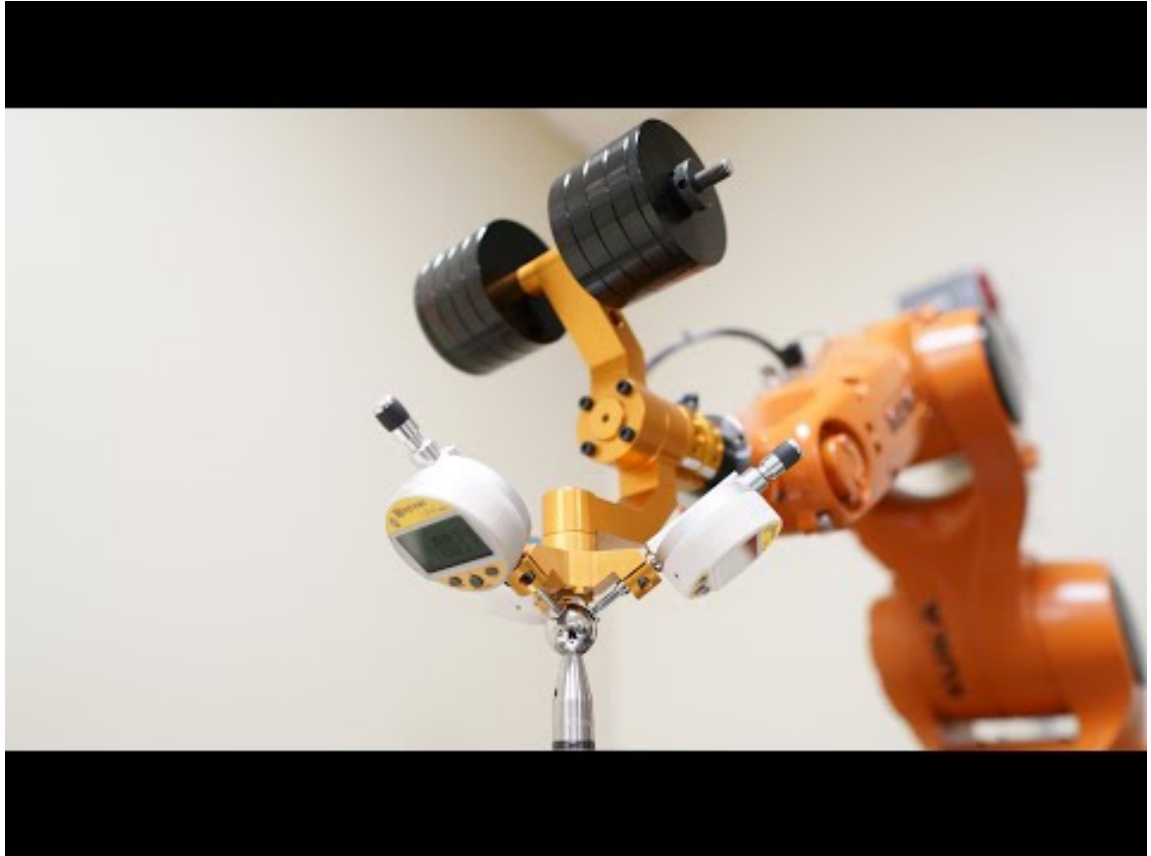
Short video of the calibration procedure

APPENDIX II

AVAILABLE PARTS AND UNITS OF THE TRICAL 3D MEASUREMENT DEVICE
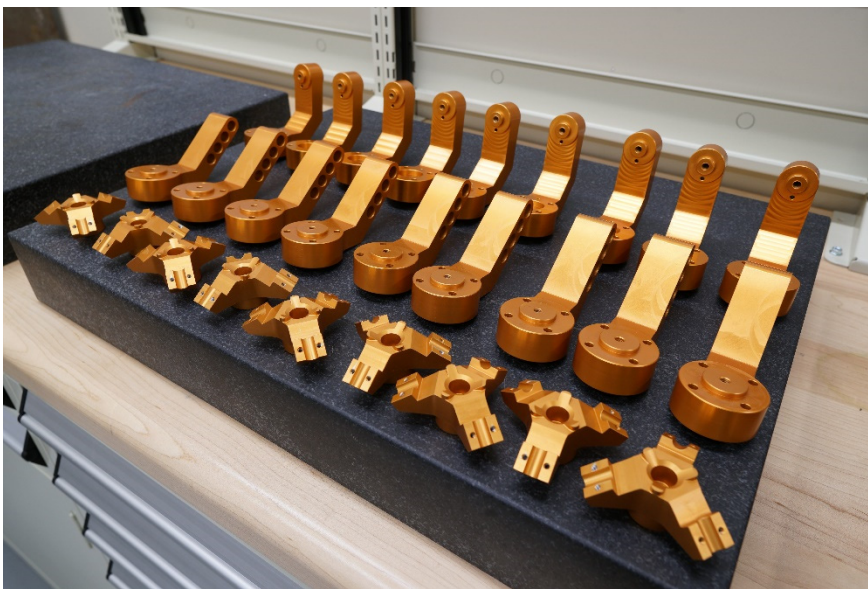

Figure II.1 TriCal measurement device

Figure II.2 TriCal measurement device components

LIST OF REFERENCES

Alici, G. and Shirinzadeh, B. 2005. A systematic technique to estimate positioning errors for robot accuracy improvement using laser interferometry based sensing. *Mechanism and Machine Theory,* vol. 40, n° 8, p. 879-906.

Aoyagi, S., Kohama, A., Nakata, Y., Hayano, Y., and Suzuki, M. 2010. Improvement of robot accuracy by calibrating kinematic model using a laser tracking system-compensation of non-geometric errors using neural networks and selection of optimal measuring points using genetic algorithm. *Intelligent Robots and Systems, 2010 IEEE/RSJ International Conference on*.

Bennett, D. J., Geiger, D., and Hollerbach, J. M. 1991. Autonomous Robot Calibration for Hand-Eye Coordination ». *The International Journal of Robotics Research,* vol. 10, n° 5, p. 550-559.

Bernhardt, R., and Albright, S. L. 1993. *Robot Calibration*, vol. 1, p. 34

Borm, J.-H., and Meng, C.-H. 1991. Determination of Optimal Measurement Configurations for Robot Calibration Based on Observability Measure. *The International Journal of Robotics Research*. vol. 10, n° 1, p. 51-63.

Chen, I. M., and Yang, G. 1997. Kinematic calibration of modular reconfigurable robots using product-of-exponentials formula. *Journal of Robotic Systems*. vol. 14, n° 11, p. 807-821.

Chen, I.-M., Yang, G., Tan, C. T., and Yeo, S. H. 2001. Local POE model for robot kinematic calibration. *Mechanism and Machine Theory*. vol. 36, n° 11-12, p. 1215-1239.

Conrad K. L., Shiakolas P. S., Yih T. C. 2000. Robotic calibration issues: accuracy, repeatability and calibration. *Control and Automation, Proceedings of the 8th Mediterranean Conference on. Rio, Patras, GREECE*

CoRoETS. (2020, April 24). *Novel, affordable device for industrial robot calibration* [Video file]. Retrieved from https://www.youtube.com/watch?v=O2vGkOy08h0&t=1s

Craig, J. J., 2005. *Introduction to robotics: mechanics and control*, vol. 3.

Denavit, J. and R. S. Hartenberg. 1955. A kinematic notation for lower-pair mechanisms based on matrices. *ASME. Journal of Applied Mechanics*, vol. 22, p. 215-221.

Driels, M. R. 1993. Using Passive End-Point Motion Constraints to Calibrate Robot Manipulators. In *Measurement, and Control, Journal of Dynamic Systems,* vol. 115, n° 3, p. 560.

Driels, M. R., and Pathre, U. S. 1990. Significance of observation strategy on the design of robot calibration experiments. *Journal of Robotic Systems*. vol. 7, n° 2, p. 197-223.

Driels, M. R., Swayze, W., and Potter, S. 1993. Full-pose calibration of a robot manipulator using a coordinate-measuring machine. *The International Journal of Advanced Manufacturing Technology,* vol. 8, n° 1, p. 34-41.

Feng, Y. L., Qu, D. K., Xu, F., and Wang, H. G. 2013. Joint Stiffness Identification and Flexibility Compensation of Articulated Industrial Robot. *Applied Mechanics and Materials,* vol. 336-338, p. 1047–1052.

Filion, A. 2015. Étalonnage de robots industriels à l''aide d''un système portable de photogrammétrie. Thesis.

Filion, A., Joubair, A., Tahan, S. A., and Bonev, I. 2018. Robot calibration using a portable photogrammetry system. *Robotics and Computer-Integrated Manufacturing*, vol. 49, p. 77-87.

Gander, W., Golub, G. H., and Strebel, R. 1994. Least-squares fitting of circles and ellipses. *BIT,* vol. 34, n° 4, p. 558-578.

Gaudreault, M., Joubair, A., and Bonev, I. 2018. Self-Calibration of an Industrial Robot Using a Novel Affordable 3D Measuring Device. *Sensors*, vol. 18, n° 10, p. 3380

Geuens, F., Van den Bossche, A., Blanckaert, P., Van den Bossche, J., and Quinet, J. F. 1997. Robot, Tool and Workcell Calibration: The Keys to Fully Integrate Off-Line Programming. *IFAC Proceedings Volumes*, vol. 30, n° 20, p. 105-110.

Gong, C., J. Yuan, and J. Ni. 2000. Nongeometric error identification and compensation for robotic system by inverse calibration. *International Journal of Machine Tools and Manufacture*, vol. 40, n° 14, p. 2119-2137.

Hanafusa, H., Yoshikawa, T., and Nakamura, Y. 1981. Analysis and Control of Articulated Robot Arms with Redundancy. *IFAC Proceedings Volumes*, vol. 14, n° 2, 1927–1932.

Hayat, A. A., Chittawadigi, R. G., Udai, A. D., and Saha, S. K. 2013. Identification of Denavit-Hartenberg Parameters of an Industrial Robot. *Advances In Robotics - AIR 2013, Proceedings of Conference on.* p. 1-6.

Hayati, S. A. 1983. Robot arm geometric link parameter estimation. *The 22nd IEEE Conference on Decision and Control.* p. 1477-1483.

Hayati, S., and Mirmirani, M. (1985). Improving the absolute positioning accuracy of robot manipulators. *Journal of Robotic Systems*, vol. 2, n° 4, p. 397-413.

Hayati, S., K. Tso, and G. Roston. 1988. Robot geometry calibration. In *Robotics and Automation, Proceedings, 1988 IEEE International Conference on*. vol.2, p. 947-951.

Heping Chen, Fuhlbrigge, T., Sang Choi, Jianjun Wang, and Xiongzi Li. 2008. Practical industrial robot zero offset calibration. *Automation Science and Engineering, IEEE International Conference on.* p. 516-521.

Horne, A. and Notash, L. 2009. Comparison of Pose Selection Criteria for Kinematic Calibration through Simulation. *Computational Kinematics, Proceedings of the 5th International Workshop.*

Jang, J. H., Kim, S. H., and Kwak, Y. K. 2001. Calibration of geometric and non-geometric errors of an industrial robot. *Robotica,* vol. 19, n° 3.

Jokiel, B., Ziegert, J. C., and Bieg, L. 2001. Uncertainty propagation in calibration of parallel kinematic machines. *Precision Engineering,* vol. 25, n° 1, p. 48-55.

Joubair, A. and I. A. Bonev. 2015b. Kinematic calibration of a six-axis serial robot using distance and sphere constraints. *The International Journal of Advanced Manufacturing Technology*, vol. 77, n° 1-4, p. 515-523.

Joubair, A., and Bonev, I. A. 2015a. Non-kinematic calibration of a six-axis serial robot using planar constraints. *Precision Engineering,* vol. 40, p. 325-333.

Joubair, A., Nubiola, A., and Bonev, I. 2013. Calibration Efficiency Analysis Based on Five Observability Indices and Two Calibration Models for a Six-Axis Industrial Robot. *SAE International Journal of Aerospace*, vol. 6, n° 1, p. 161-168.

Joubair, A., Slamani, M., and Bonev, I. A. 2012. A novel XY-Theta precision table and a geometric procedure for its kinematic calibration. *Robotics and Computer-Integrated Manufacturing,* vol. 28, n° 1, p. 57-65.

Joubair, Ahmed. 2012. Contribution a l''amelioration de la précision absolue des robots paralleles. Thesis

Judd, R. P., and Knasinski, A. B. 1990. A technique to calibrate industrial robots with experimental verification. *Robotics and Automation, IEEE Transactions on,* vol. 6, n° 1, p. 20–30.

Kamali, K., Joubair, A., Bonev, I. A., and Bigras, P. 2016. Elasto-geometrical calibration of an industrial robot under multidirectional external loads using a laser tracker. *Robotics and Automation (ICRA), 2016 IEEE International Conference on*, p. 4320-4327.

Kamali, K., Joubair, A., Bonev, I. A., and Bigras, P. 2016. Elasto-geometrical calibration of an industrial robot under multidirectional external loads using a laser tracker. *2016 IEEE International Conference on Robotics and Automation (ICRA)*.

Kastner T., Röfer T., and Laue T. 2015. Automatic Robot Calibration for the NAO. In: *Bianchi R., Akin H., Ramamoorthy S., Sugiura K. RoboCup 2014: Robot World Cup XVIII. RoboCup 2014*, vol. 8992. Springer, Cham

Khalil, W., and Besnard, S. 2002. Geometric Calibration of Robots with Flexible Joints and Links. *Journal of Intelligent and Robotic Systems,* vol. 34, n° 4, p. 357-379.

Khalil, W., and Gautier, M. 1985. Identification of Geometric Parameters of Robots. *IFAC Proceedings Volumes*, vol. 18, n° 16, p. 27-30.

Khalil, W., Gautier, M., and Enguehard, C. 1991. Identifiable Parameters and Optimum Configurations for Robots Calibration. *Robotica,* vol. 9, n° 1, p. 63.

Khosla, P., and Kanade, T. 1985. Parameter identification of robot dynamics. *24th IEEE Conference on Decision and Control.* p. 1754-1760.

Klema, V., and Laub, A. 1980. The singular value decomposition: Its computation and some applications. In *Automatic Control, IEEE Transactions on.* vol. 25, n° 2, p. 164-176.

Kucuk, S., and Bingul, Z. 2003. Robot workspace optimization based on the global conditioning index. *IFAC Proceedings Volumes.* vol. 36, n° 7, p. 117-122.

L. Beyer and J. Wulfsberg. 2004. Practical robot calibration with ROSY. *Robotica*, vol. 22, pp. 505-51

Lau, K., Hocken, R., and Haynes, L. 1985. Robot performance measurements using automatic laser tracking techniques. *Robotics and Computer-Integrated Manufacturing,* vol. 2, n° 3-4, p. 227-236.

Levenberg, K. 1944. A method for the solution of certain non-linear problems in least squares. *Quarterly of Applied Mathematics,* vol. 2, n° 2, p. 164-168.

Li, P., Zeng, R., Xie, W., and Zhang, X. 2018. Relative posture-based kinematic calibration of a 6-RSS parallel robot by optical coordinate measurement machine. *International Journal of Advanced Robotic Systems,* vol. 15, n° 2, p. 1-14.

Lightcap, C., Hamner, S., Schmitz, T., and Banks, S. 2008. Improved Positioning Accuracy of the PA10-6CE Robot with Geometric and Flexibility Calibration. *Robotics, IEEE Transactions on,* vol. 24 n° 2, p. 452–456.

Marquardt, D. W. 1963. An Algorithm for Least-Squares Estimation of Nonlinear Parameters. *Journal of the Society for Industrial and Applied Mathematics,* vol. 11, n° 2, p. 431-441.

Mecademic, Meca500 - Ultracompact six-axis industrial robot arm. Available online: https://www.mecademic.com/products/Meca500-small-robot-arm

Nadeau, N. A., Bonev, I. A., and Joubair, A. 2019. Impedance Control Self-Calibration of a Collaborative Robot Using Kinematic Coupling. *Robotics,* vol. 8, n° 2, p. 33.

Nahvi, A. and J. M. Hollerbach. 1996. The noise amplification index for optimal pose selection in robot calibration. In *Robotics and Automation. Proceedings of the 1996 IEEE International Conference on.* vol. 1 p. 647-654.

Nahvi, A., Hollerbach, J. M., and Hayward, V. 1994. Calibration of a parallel robot using multiple kinematic closed loops. In *Robotics and Automation*, *Proceedings of the 1994 IEEE International Conference on.*

Nelder, J. A., and Mead, R. 1965. A Simplex Method for Function Minimization. *The Computer Journal,* vol. 7, n° 4, p. 308-313.

Newman, W. S., Birkhimer, C. E., Horning, R. J., and Wilkey, A. T. 2000. Calibration of a Motoman P8 robot based on laser tracking. In *Robotics and Automation Proceedings 2000 ICRA, IEEE International Conference on.*

Nguyen, H.-N., J. Zhou, and H.-J. Kang. 2015. A calibration method for enhancing robot accuracy through integration of an extended Kalman filter algorithm and an artificial neural network. *Neurocomputing*, vol. 151, n° 3, p. 996-1005.

Nguyen, H.-N., Zhou, J., Kang, H.-J., and Ro, Y.-S. 2013. Robot Geometric Parameter Identification with Extended Kalman Filtering Algorithm. *Emerging Intelligent Computing Technology and Applications,* p. 165–170.

Nubiola, A. et I. A. Bonev. 2013. Absolute calibration of an ABB IRB 1600 robot using a laser tracker. *Robotics and Computer-Integrated Manufacturing*, vol. 29, n° 1, p. 236-245.

Nubiola, A., Slamani, M., Joubair, A., and Bonev, I. A. 2014. Comparison of two calibration methods for a small industrial robot based on an optical CMM and a laser tracker. *Robotica,* vol. 32, n° 3, p. 447-466.

Nubiola, Albert. 2011. Calibration of a serial robot using a laser tracker ». Thesis on matrices. *ASME. Journal of Applied Mechanics*, vol. 22, p. 215-221.

Pott, A., Kecskeméthy, A., and Hiller, M. 2007. A simplified force-based method for the linearization and sensitivity analysis of complex manipulation systems. *Mechanism and Machine Theory,* vol. 42, n° 11, p. 1445-1461.

Puskorius, G., and Feldkamp, L. 1987. Global calibration of a robot/vision system. In *Robotics and Automation, Proceedings, 1987 IEEE International Conference on*.

RoboDK Offline Simulation and Programming Home Page [Computer software]. Available online: https://robodk.com/

Savoure, L., Maurine, P., Corbel, D., and Krut, S. 2006. An improved method for the geometrical calibration of parallelogram-based parallel robots. In *Robotics and Automation, Proceedings 2006 IEEE International Conference on, ICRA 2006.*

Schröer, K., Albright, S. L., and Grethlein, M. 1997. Complete, minimal and model-continuous kinematic models for robot calibration. *Robotics and Computer-Integrated Manufacturing,* vol. 13, n° 1, p. 73-85.

Slamani, M., Nubiola, A., and Bonev, I. 2012. Assessment of the positioning performance of an industrial robot. *Industrial Robot: An International Journal,* vol. 39, n° 1, p. 57-68.

Stone, H., Sanderson, A., and Neuman, C. 1986. Arm signature identification. In *Robotics and Automation Proceedings. 1986 IEEE International Conference on*. p. 41-48.

Sun, Y. and Hollerbach, J. M. 2008a. Active robot calibration algorithm. In *Robotics and Automation, 2008 IEEE International Conference on.*

Sun, Y. and Hollerbach, J. M. 2008b. Observability index selection for robot calibration. In *Robotics and Automation, 2008 IEEE International Conference on.*

Urrea, C., Cortés, J., and Pascal, J. 2016. Design, construction and control of a SCARA manipulator with 6 degrees of freedom. *Journal of Applied Research and Technology,* vol. 14, n° 6, 396–404.

Whitney, D. E., C. A. Lozinski, and J. M. Rourke. 1986. Industrial Robot Forward Calibration Method and Results. *Journal of Dynamic Systems, Measurement, and Control*, vol. 108, n° 1, p. 1-8.

Zak, G., Benhabib, B., Fenton, R. G., and Saban, I. 1994. Application of the Weighted Least Squares Parameter Estimation Method to the Robot Calibration. *Journal of Mechanical Design,* vol. 116, n° 3, p. 890.

Zhuang, H., Wang, L. K., and Roth, Z. S. 1993. Error-model-based robot calibration using a modified CPC model. *Robotics and Computer-Integrated Manufacturing*. vol. 10, n° 4, p. 287-299.

Zhuang, H., Wang, L, and Roth, Z.S.1993. Simultaneaous calibration of a robot and a hand-mounted camera. In *Robotics and Automation, proceedings, IEEE International Conference*